The Journal of Chemical Physics

RESEARCH ARTICLE | APRIL 28 2025

Complete exciton Hamiltonian for photosynthetic pigment–protein complexes

Special Collection: David Jonas Festschrift

Austėja Mikalčiūtė ; Darius Abramavičius

J. Chem. Phys. 162, 164109 (2025)
https://doi.org/10.1063/5.0258368

The Journal
of Chemical Physics

ARTICLE

pubs.aip.org/aip/jcp

Complete exciton Hamiltonian for photosynthetic pigment–protein complexes

Cite as: J. Chem. Phys. 162, 164109 (2025); doi: 10.1063/5.0258368
Submitted: 16 January 2025 • Accepted: 21 March 2025 •
Published Online: 28 April 2025

Austėja Mikalčiūtė and **Darius Abramavičius**[a)]

AFFILIATIONS

Institute of Chemical Physics, Faculty of Physics, Vilnius University, Sauletekio al. 9-III, LT-10222 Vilnius, Lithuania

Note: This paper is part of the JCP Special Topic, David Jonas Festschrift.
[a)] **Author to whom correspondence should be addressed:** darius.abramavicius@ff.vu.lt

ABSTRACT

The standard exciton theory used for describing spectroscopy of molecular complexes usually assumes an infinite exciton lifetime, coming from complete isolation of Hamiltonian blocks describing a different number of excitations. We focus on extending the model by including environment-induced non-resonant couplings in the Hamiltonian, which couple different numbers of excitons. We analyze their impact on the absorption spectra of two small light-harvesting complexes: Fenna–Matthews–Olson and fucoxanthin–chlorophyll protein. Quantum mechanics calculations of the pigment properties, combined with an electrostatic description of the protein, allowed us to construct the full Hamiltonian and calculate the exciton lifetimes and the absorption spectra. The resulting off-resonant terms in the Hamiltonian are significant and cannot be excluded from calculations of linear (or non-linear) spectra.

I. INTRODUCTION

Photosynthesis serves as one of the key processes for sustaining life on Earth. For researchers, photosynthetic pigment–protein complexes are fundamental model systems for energy absorption, transfer, and conversion.[1,2] As the quantum efficiency of the photosynthetic apparatus is high, discovering the underlying mechanisms of various dynamic processes might provide solutions to more sustainable energy transfer and production.[3–5] The collection of sunlight energy is performed in light harvesting complexes (LHC) of various pigment–protein complexes; these “antennas” absorb in the visible spectral region due to chlorophyll-like pigments and carotenoids. Multiple LHCs surround the core antenna complexes, which are located near the reaction center,[6] which is responsible for charge separation.[7–9]

These light harvesting complexes have a wide variety of amino acid sequences, which define the superstructure formation of proteins.[10–12] In addition, various types of accessory ligands,[13] pigment types,[14,15] and their spatial configurations make each pigment–protein complex unique. Detailed studies of these complexes became available only after determining their molecular structures by X-ray diffraction (XRD).[16–19] Since then, many studies have tried to capture both experimentally and theoretically the underlying nature of light absorption and energy transfer mechanisms.[20–25]

The first light-harvesting antenna fully captured by XRD was the Fenna–Matthews–Olson (FMO) complex from green sulfur bacteria.[26] The FMO complex is found in a trimeric form and poses a C_3 symmetry. Each monomer contains seven or eight bacteriochlorophyll (BChl) *a* molecules. It is one of the most studied pigment–protein complexes: linear[27–29] and transient absorption,[28] photon echo,[30,31] hole-burning,[29,32,33] and linear[34,35] and circular dichroism[34,36] spectra are available, as well as many theoretical studies,[37–40] which describe excitation coherent dynamics and relaxation. More specifically, Wending *et al.*[36] described absorption and linear and circular dichroism spectra at 77 K. The absorption spectrum has five partially overlapping bands at 790, 800, 804, 813, and 824 nm. The spectra were explained using the exciton model within the point-dipole approximation, accounting for broadening mechanisms. The exciton ultrafast dynamics was characterized using the most advanced two dimensional electronic spectroscopy (2DES) approach on a femtosecond–picosecond timescale using unprecedented resolution.[41–44] 2DES with full polarization control provides an accurate description of the electronic structure and population dynamics in the complex. The time evolution of the spectral structure, covering time scales from tens of femtoseconds up to a nanosecond, revealed the energy flow in FMO.[42,44,45] 2DES has revealed quantum coherences with timescales comparable to those of energy-transfer processes. These observations have led to a debate regarding the states that give rise to the coherences and whether the presence of these coherences has implications for photosynthetic light harvesting.[46] Assignments of the observed quantum coherences to electronic, vibronic, or vibrational types have been made available by using coherence tracing algorithms.[47–49]

Modeling of the experimental data based on molecular structure has been the ultimate goal of the theory. Adolphs and Renger[37] devised an electrostatic method to calculate optical transition energies from crystallographic structure, which has the capacity of the agreement with experiments. They found that the chromophore transition energies shift due to charged amino acids and ligands. Newer theoretical studies of FMO complexes utilize more complicated methodologies, which account for protein motion using quantum mechanics/molecular mechanics (QM/MM) simulations with the effective fragment potential simulations. Kim *et al.*[38] were able to improve Hamiltonian calculations in agreement with previous literature values and obtained the quantitative match of absorption spectra. A similar study has been carried out by Huai *et al.*[39] for mutants of FMO from *Chlorobaculum tepidum* and *Prosthecochloris aestuarii*. Reinot *et al.* have determined that a single point mutation, W183 in *Chlorobaculum tepidum*, changes the absorption spectra of FMO from type 2 (where the 806 nm band is more pronounced) to type 1 (where the 815 nm band is more pronounced). These calculations raise the importance of protein amino acid sequence and its conformation to the absorption spectra. In addition, calculations revealed the wavelength-dependent distributions of exciton lifetimes in the femtosecond to picosecond time frame. The lifetime distributions offer insight into the interpretation of resonant hole-burned (HB) spectra, kinetic traces in two-dimensional (2D) electronic spectroscopy experiments, and widely used global analyses in fitting data from transient absorption experiments.[40]

However, a refinement of quantum chemical calculations is usually necessary to yield the correct coupling pattern and correct chromophore transition energies in the sense of matching the experimental spectra. This implies that primary quantum chemical calculations may carry systematic errors, although it remains unclear to what extent. Another possibility is related to still approximate exciton modeling, where off-resonant terms in the Hamiltonian are usually neglected. Essentially, the widely used Frenkel exciton model usually conserves the number of excitons, which is still an approximation. It is important to point out that additional off-resonant couplings, which couple excited states with the ground state, appear also purely due to electrostatic intermolecular interactions in the same form as the resonant couplings.

In this paper, we extend the standard exciton model, including the environment-induced off-resonant inter-molecular couplings, and use the resulting Hamiltonian to calculate the variation of absorption spectra of light-harvesting complexes. The pigments were first modeled at the QM level, while their transition energies were adjusted due to electrostatic interactions with proteins. The full non-resonant excitonic Hamiltonian is then used to calculate the exciton transfer rates, their lifetimes, and the absorption spectra of the complexes. We find that the excitonic non-resonant coupling amplitudes lead to finite exciton lifetimes, shift the absorption spectra to higher energies, and affect the spectral line shapes.

II. QUANTUM THEORY OF COUPLED MOLECULES

The core element of the quantum description of a molecular system is the energy operator—the Hamiltonian. The most complete form of the operator (without spin-related interactions) for electrons consists of all possible electrostatic interactions involving all electrons and all nuclei (i.e., all charged particles). We start from the general Hamiltonian of interacting charges in atomic units,

$$\hat{H}_S = \hat{K}(\{\boldsymbol{r}_\alpha\}) + \frac{1}{2}\sum_{\alpha\beta}^{\alpha\neq\beta}\frac{1}{|\boldsymbol{r}_\beta - \boldsymbol{r}_\alpha|} - \sum_{n\alpha}\frac{q_n}{|\boldsymbol{R}_n - \boldsymbol{r}_\alpha|} + \frac{1}{2}\sum_{nm}^{n\neq m}\frac{q_n q_m}{|\boldsymbol{R}_n - \boldsymbol{R}_m|}, \tag{1}$$

where $\{\boldsymbol{r}_\alpha\}$ denotes the full list $\boldsymbol{r}_1, \boldsymbol{r}_2, \ldots$ of electron coordinates and $\boldsymbol{R}_n$ denotes nuclei with charges q_n. $\hat{K}(\{\boldsymbol{r}_\alpha\})$ is the kinetic energy operator for all electrons; the second term in the equation denotes the electron–electron interaction, the third term is due to the electron–nuclei interaction, and the last term (not the operator) is the nuclei–nuclei interaction energy. Next, electrons and nuclei are grouped into molecules, where electron exchange between different molecules will be ignored. The Hamiltonian is then organized into separate Hamiltonians of the chromophores and the remaining intermolecular interactions,

$$\hat{H}_S = \sum_{m}^{N}\hat{H}_m + \frac{1}{2}\sum_{m,m'}^{m\neq m'} V_{mm'}. \tag{2}$$

From the general definition, we find the chromophoric Hamiltonians

$$\hat{H}_m = \hat{K}(\{\boldsymbol{r}_\alpha^{(m)}\}) + \frac{1}{2}\sum_{\alpha\beta}^{\alpha\neq\beta}\frac{1}{\left|\boldsymbol{r}_\beta^{(m)} - \boldsymbol{r}_\alpha^{(m)}\right|} - \sum_{n\alpha}\frac{q_n}{\left|\boldsymbol{R}_n^{(m)} - \boldsymbol{r}_\alpha^{(m)}\right|} + \frac{1}{2}\sum_{nm}^{n\neq m}\frac{q_n q_m}{\left|\boldsymbol{R}_n^{(m)} - \boldsymbol{R}_m^{(m)}\right|}, \tag{3}$$

where $\boldsymbol{r}_\alpha^{(m)}$ and $\boldsymbol{R}_n^{(m)}$ denote electrons and nuclei belonging solely to molecule m. Intermolecular interaction is then given by electron–electron and electron–nuclei interactions as well as nuclear–nuclear repulsion of different molecules:

$$V_{mm'} = \sum_{\alpha\beta}\frac{1}{\left|\boldsymbol{r}_\beta^{(m)} - \boldsymbol{r}_\alpha^{(m')}\right|} + \sum_{nk}\frac{q_n q_k}{\left|\boldsymbol{R}_n^{(m)} - \boldsymbol{R}_k^{(m')}\right|} - \sum_{n\alpha}\left(\frac{q_n}{\left|\boldsymbol{R}_n^{(m')} - \boldsymbol{r}_\alpha^{(m)}\right|} + \frac{q_n}{\left|\boldsymbol{R}_n^{(m)} - \boldsymbol{r}_\alpha^{(m')}\right|}\right). \tag{4}$$

In this expression, the sum over n or m involves only the sum over nuclei of the particular chromophores, while the sum over electrons involves only particular electrons of other molecules. Explicit expressions of Hamiltonian terms can be found in the Appendix.

Next, we follow the standard exciton model formulation; however, some additional coupling terms will be included. In the first step, the basis states for the quantum description are formulated. It is assumed that electronic stationary states of separate molecules in their optimal geometry are available from independent calculations. Hence, we introduce the many-electron stationary molecular states,

$$\hat{H}_m \Psi_k(\{r_\alpha^m\}) = E_k^{(m)} \Psi_k(\{r_\alpha^m\}), \tag{5}$$

where $\hat{H}_m$ is the electronic Hamiltonian of molecule m, $\{r_\alpha^m\}$ denotes the list of all electrons of that molecule, and $\Psi_k(\{r_\alpha^m\})$ is the real-space wave function of the molecule in electronic state k, whose energy is $E_k^{(m)}$. The lowest energy state is the *ground* state. By switching to bra-ket notation, we write it as $|g_m\rangle \equiv \Psi_g(\{r_\alpha^m\})$. The next higher-energy electronic state is the *excited* state under consideration, $|e_m\rangle \equiv \Psi_e(\{r_\alpha^m\})$. Other electronic excited states can be included in the same way. Considering optical excitations, these states are assigned to specific chromophoric groups of molecules. For chlorophylls and bacteriochlorophylls, these are related to excitations of the central chlorin rings of the molecules.

These molecular states are used as the basis states to construct the Hamiltonian matrix of a molecular complex, composed of such molecules following the Heitler–London formulation, which holds perfectly when electron exchange among molecules is not possible. Hence, we denote the collective ground state constructed as a direct product of the ground molecular states

$$|G\rangle = \Pi_m^N |g_m\rangle, \tag{6}$$

and a block of excited states representing an excitation of a specific chromophore in the complex to its excited state $|e_m\rangle$,

$$|X_m\rangle = |e_m\rangle \Pi_k^{k\neq m} |g_k\rangle. \tag{7}$$

The complete wave function of the complex is then given by a superposition of such basis states,

$$\Phi = c_g|G\rangle + \sum_m c_m |X_m\rangle. \tag{8}$$

This resulting wave function must satisfy the Schrödinger equation of the whole molecular complex, i.e.,

$$\hat{H}_S \Phi = \varepsilon \Phi, \tag{9}$$

with the complete Hamiltonian

$$\hat{H}_S = \sum_m^N \hat{H}_m + \frac{1}{2} \sum_{m,m'}^{m\neq m'} V_{mm'}, \tag{10}$$

where $V_{mm'}$ is the electrostatic interaction energy operator between molecules m, m'. This leads to the matrix eigenvalue equation

$$\left(\hat{H}_S\right)_{kl} c_l = \varepsilon c_k. \tag{11}$$

The Hamiltonian matrix elements H_{kl} involves various types of configurations of states. The diagonal matrix elements are the site energies, which become shifted from the transition energies of independent chromophores due to electrostatic interactions with all other chromophores ($k \neq g$): $\left(\hat{H}_S\right)_{kk} = \langle X_k|\hat{H}_s|X_k\rangle$. Resonant couplings lead to exciton hopping and delocalization ($k \neq l$, $k \neq g, l \neq g$) $\left(\hat{H}_S\right)_{kl} = \langle X_k|\sum_m^N \hat{H}_m + \frac{1}{2}\sum_{m,m'}^{m\neq m'} V_{mm'}|X_l\rangle$. Together with the shifted ground state (also due to interactions with neighboring chromophores), $\left(\hat{H}_S\right)_{gg} = \langle G|\sum_m^N \hat{H}_m + \frac{1}{2}\sum_{m,m'}^{m\neq m'} V_{mm'}|G\rangle$. These elements form the basis of the Frenkel exciton model, which is block-diagonal, i.e., conserves the number of excitations, and is considered in most of the applications.

These elements can be expressed more explicitly. The ground state energy can be written as

$$\left(\hat{H}_S\right)_{gg} = \sum_m^N E_g^{(m)} + \frac{1}{2} \sum_{m,m'}^{m\neq m'} V_{mm'}^{(00)}, \tag{12}$$

where $V_{mm'}^{(00)} = \langle g_m g_{m'}|V_{mm'}|g_m g_{m'}\rangle$ is the full electrostatic interaction between two molecules being in their ground states; for the excited states, we find

$$\left(\hat{H}_S\right)_{kk} = E_e^{(k)} + \sum_m^{m\neq k} E_g^{(m)} + \sum_m^{m\neq k} V_{km}^{(10)} + \frac{1}{2} \sum_{mm'}^{m'\neq k, m\neq k} V_{mm'}^{(00)}, \tag{13}$$

where $V_{mm'}^{(10)} = \langle e_m g_{m'}|V_{mm'}|e_m g_{m'}\rangle$ represents the full electrostatic interaction between molecules m and m', where m is in its excited state, while m' is in the ground state. Finally, the resonant coupling ($k \neq l$)

$$\left(\hat{H}_S\right)_{kl} = \langle e_k g_l|V_{kl}|e_l g_k\rangle \equiv J_{kl} \tag{14}$$

is the electrostatic interaction between the transition charge densities. These elements can be related to specific charge densities as presented in the Appendix.

However, this set of coupling elements is not final. We additionally bring forward one more set of elements, which are non-resonant and connect the ground and excited states, i.e., ($k \neq g$),

$$\left(\hat{H}_S\right)_{gk} = \sum_m^{m\neq k} \langle g_k g_m|V_{mk}|e_k g_m\rangle \equiv L_k. \tag{15}$$

These elements can also be written in terms of the same charge densities as above (see Appendix). They non-trivially mix excited states of the complex with the electronic ground state.

Using the electronic ground state as a reference, we write the following Hamiltonian matrix of the aggregate in the above-defined basis of product states,

$$\hat{H}_S = \begin{pmatrix} 0 & L_1 & L_2 & \dots & L_N \\ L_1 & J_{11} & J_{12} & \dots & J_{1N} \\ L_2 & J_{12} & J_{22} & \dots & J_{2N} \\ \dots & \dots & \dots & \dots & \dots \\ L_N & J_{N1} & J_{N2} & \dots & J_{NN} \end{pmatrix}. \tag{16}$$

All the matrix elements have been defined earlier, and the site energies are now written with respect to the ground state energy,

$$J_{nn} = E_e^{(n)} - E_g^{(n)} + \sum_m \left(V_{nm}^{(10)} - V_{nm}^{(00)}\right). \tag{17}$$

Notice that the sum corresponds to the difference in the electrostatic interaction of the molecule *n* with the equilibrium environment when the molecule changes the state from the ground state to its excited state.

Eigenstates of this Hamiltonian are stationary states of the aggregate. These states are shifted from the Frenkel exciton states, where $L_n = 0$ is assumed. In addition, notice that the non-resonant solvent molecules (or proteins) can be included when calculating energy shifts and *L*-type couplings because these involve electrostatic interactions with the ground state properties of the environment. Accordingly, the sums in Eqs. (15) and (17) may be extended over the whole "universe," e.g., the protein environment.

III. METHODS

A. Hamiltonian construction

Bacteriochlorophyll *a* (BChl *a*) molecule structure was extracted from chain A of the 6MEZ FMO Protein Data Bank (PDB) structure (chromophore id: 401)[17] using the PyMOL molecular visualization system.[50] Then hydrogens were added to the molecule with GaussView software.[51] Quantum mechanical (QM) calculations were performed using Gaussian software:[52] density functional theory (DFT) was used for ground state calculations and time dependent DFT (TD-DFT) for excited state calculations. The approaches were based on the CAM-B3LYP functional and the 6-31G(d) basis set. The main purpose of QM modeling was to obtain the wavefunction of the pigments and to construct the atomic point charges from the output of the calculations. BChl *a* was modeled without a phythyl tail, as it is not of significant importance for optically active electronic states of chlorophyll-like molecules. First, the ground state (S_0) geometry optimization and frequency calculations were performed to ensure that the molecular geometry converged to a reasonable structure and that no imaginary frequencies were found. The S_0 optimized geometry was used as the starting configuration for excited states S_1 and S_2 geometry optimizations and their frequency calculations—their final structures were used to calculate excited states electronic charge densities at the corresponding potential energy minima. The permanent and transition charge densities for the two lowest excited states (S_1 and S_2), which are usually denoted as Q_y and Q_x, were parameterized using Multiwfn software,[53] which constructed atomic point charges from electrostatic potential surfaces based on the Gaussian output files. The pigment structures obtained from Gaussian were mapped to the original PDB structures using rotation matrices generated by Chimera software[54] to find one-to-one correspondence between atoms in pigments between the QM and the original PDB structures (as the labeling and coordinate systems in them differ). Then the partial atomic charges as realized in Multiwfn were assigned to the pigment atoms in the original PDB structure geometry. Note that the renormalization of charges was performed to match experimental transition dipole moments of BChl *a*: $|\mu_{01}^{QM}| = 7.49 \rightarrow 7.25$ D.[55]

Two different FMO structures were considered: 6MEZ[17] and 3EOJ,[56] both from *Prosthecochloris aestuarii* (Fig. 1). For proteins, the hydrogens were added, and protein atom charges representing thermal equilibrium were generated using the PDB2PQR software package[57] using either PARSE[58] or AMBER[59] force fields (FFs) (both results are presented) at pH = 8. The net protein charge becomes non-zero (2−). To compensate for it, two additional Na^+ ions were included using Chimera[54] software.

For comparison, we additionally study a small complex made of Chl pigments—the fucoxanthin–chlorophyll protein (FCP).[19,60–65] FCP is a unique LHC of marine photosynthetic diatoms—unicellular photosynthesis carrying organisms that account for around 20 percent of total primary production on Earth.[66] FCP contains chlorophylls (Chl) *a* and *c*, the ratio of which may vary from complex to complex: FCP discovered by Wang *et al.* has seven Chl *a* and two Chl *c*.[19] Typically, all Chl *a* in FCP forms a rather homogeneous Gaussian-shaped peak at 672 nm, while Chl *c* absorbs at 636 nm and shows a significantly smaller peak.[67] Due to the late determination of the atomic structure, there are still only a few modeling studies present to this day compared to other LHCs.[68–70] However, for the present study, this is just another small-sized complex involving Chl pigments. Hence, the same type of parameterization and DFT/TD-DFT calculation was performed for chlorophyll *a* and *c* molecules, which are the main pigments in FCP. The renormalization for chlorophyll dipole moments was used the same as in Ref. 68: Chl *a* – $|\mu_{01}^{QM}| = 5.26 \rightarrow 5.47$ D.[55] According to the experimental absorption spectra of Chl *a* and *c*,[71] it can be estimated that the ratio of Chl *a* to Chl *c* Q_y transition dipole moments is around 1.58; therefore, the mean of Chl *c* transition dipole moments was scaled accordingly. The same scaling factor was applied to other Chl

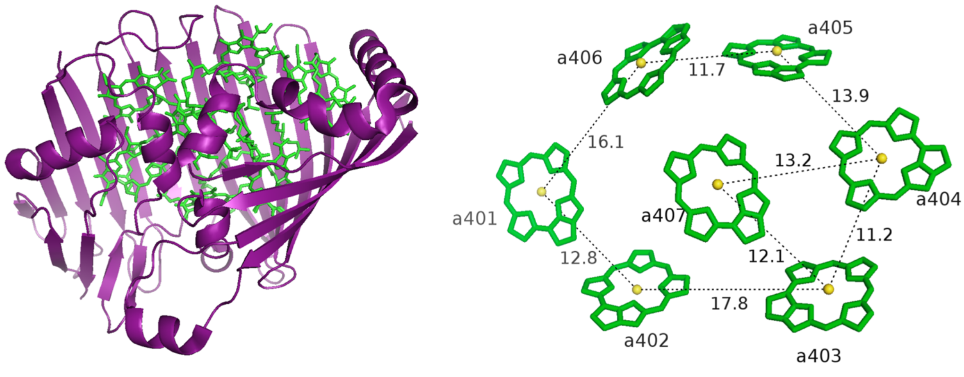

(a) (b)

FIG. 1. FMO 6MEZ structure: (a) protein and bacteriochlorophylls surrounded by it and (b) bacteriochlorophylls displayed as only their porphyrin rings with distances between their central Mg atoms in Å.

dipole moments as well. Analogical protein reconstruction was then repeated for 6A2W FCP protein.

The full Hamiltonians of the systems were calculated using locally built Quantum Correlation Functions and Propagators (QCFP) software. Using the TrEsp methodology with a dielectric constant of $\epsilon = 2$, the pigment–pigment resonant interaction energy between excitations is given by

$$J_{mn} = \frac{1}{4\pi\epsilon\epsilon_0}\sum_{ij}\frac{q_{ni}^{ge}q_{mj}^{ge}}{|\vec{r}_{ni} - \vec{r}_{mj}|}, \tag{18}$$

where q_{ni}^{eg} are the corresponding transition charges of molecule n and $\vec{r}_{ni}$ are their positions. Pigment excitation energy shifts due to the protein environment are given by

$$\Delta E_{nn} = \frac{1}{4\pi\epsilon\epsilon_0}\sum_{k}\sum_{ij}\frac{(q_{ni}^{ee} - q_{ni}^{gg})q_{kj}^{gg}}{|\vec{r}_{ni} - \vec{r}_{kj}|}, \tag{19}$$

where q_{ni}^{ee} and q_{ni}^{gg} are the excited state and the ground state molecular charges, respectively. It is important to note that in our work we did not use the TD-DFT obtained excited state energies of the pigments as the base excitation energies: it is well known that TD-DFT usually does not produce these properties in a quantitative agreement with experiments. Therefore, we used experimental BChl *a*,[72] Chl *a*,[73,74] and Chl *c*[75] values in diethyl-ether for Q_y and Q_x excitations as the base excitation energies with shifts calculated from Eq. (19) for each pigment. Excited pigment coupling with the global ground state, i.e., the non-resonant coupling matrix elements L, is obtained as electrostatic interactions between the ground state and transition charges of the molecules (see Appendix),

$$L_{gn} = \frac{1}{4\pi\epsilon\epsilon_0}\sum_{k}\sum_{ij}\frac{q_{ni}^{ge}q_{kj}^{gg}}{|\vec{r}_{ni} - \vec{r}_{kj}|}. \tag{20}$$

These parameters construct the system Hamiltonian, as formulated in Sec. II. Further diagonalization of the Hamiltonian yields the complete set of exciton states (and the updated ground state).

B. Fluctuations of the aggregate Hamiltonian and exciton relaxation

The standard fluctuating exciton model can be straightforwardly extended to describe exciton transport as well as exciton decay in the present exciton model. The model is extended by appending the vibrational (and phonon) degrees of freedom as the harmonic bath linearly coupled with the chromophore transition energies. Accordingly, the fully extended Hamiltonian is given by[76,77]

$$\hat{H}_{full} = \hat{H}_S + \hat{H}_{S-Ph} + \hat{H}_{Ph}. \tag{21}$$

Here

$$\hat{H}_{Ph} = \frac{1}{2}\sum_{p}\omega_p(P_p^2 + Q_p^2), \tag{22}$$

lists all phonons as harmonic oscillators with frequencies ω_p, dimensionless momenta P_p, and coordinates Q_p. The system–phonon interaction is defined by the shifted oscillator model, where the oscillator equilibrium in the electronic excited state is shifted from that of the ground state. This yields

$$\hat{H}_{S-Ph} = \sum_{m}\sum_{p}\omega_p d_{pm}Q_p|X_m\rangle\langle X_m|. \tag{23}$$

Here, summation over m includes only the excited state manifold. Assuming that all molecules are statistically identical, while independent (uncorrelated), we find the single molecular spectral density function, characterizing all chromophores,

$$C''(\omega) = \pi\sum_{p}\omega_p^2 s_p[\delta(\omega - \omega_p) - \delta(\omega - \omega_p)]. \tag{24}$$

Here, $s_p = d_{pm}^2/2$ are the dimensionless Huang–Rhys parameters (we assume them to be the same for all chromophores). They are directly related to the chromophore reorganization energies $\lambda = \sum_p s_p\omega_p$.

This model allows for the calculation of the dephasing and excitation transfer rates, which in the present formulation involves the electronic ground state just like any other arbitrary state. While in the site-basis, the fluctuations affect only excited states; the ground state becomes involved via L couplings.

The problem is most conveniently represented in the eigenstate basis of the system Hamiltonian [see, e.g., (11)]. The transformation yields fluctuations for all transformed Hamiltonian elements,

$$(H_{S-Ph}^{(e)})_{kl} = \sum_{p}\left(\sum_{m}c_{mk}c_{ml}d_{pm}\right)\omega_p Q_p, \tag{25}$$

where the sum over m involves only excited states, while eigenstate indices k, l include all states (including the ground state). The superscript (e) denotes the eigenstate basis, where the system Hamiltonian is diagonal.

The essential components for the relaxation are the fluctuation correlation functions (in the Heisenberg picture),

$$\begin{aligned} C_{ij,kl}^{(e)}(t) &= \mathrm{Tr}_B\left[\left(H_{S-Ph}^{(e)}(t)\right)_{ij}(H_{S-Ph}^{(e)})_{kl}\rho_0\right] \\ &= \Lambda_{ijkl}C(t), \end{aligned} \tag{26}$$

where Tr_B is the trace over environment degrees of freedom, $\Lambda_{ijkl} = \sum_n c_{ni}c_{nj}c_{nk}c_{nl}$ is the exciton overlap tensor, and the site-fluctuation correlation function is expressed using the above-defined spectral density,

$$\begin{aligned} C(t) &\equiv \sum_{p} d_{pm}^2\omega_p^2\,\mathrm{Tr}\left[Q_p(t)Q_p\rho_0\right] \\ &= \int_{-\infty}^{\infty}\frac{d\omega}{2\pi}e^{-i\omega t}(1 + \coth(\beta\omega/2))C''(\omega). \end{aligned} \tag{27}$$

It is convenient to define its Fourier–Laplace transform,[78]

$$\begin{aligned} M(\omega) &= \int_0^{\infty}\mathrm{d}te^{i\omega t}C(t) \\ &= \frac{1}{2}(1 + \coth(\beta\omega/2))C''(\omega) \\ &\quad + \frac{i}{2\pi}\fint_{-\infty}^{\infty}\frac{ds}{s}C''(s + \omega)(1 + \coth(\beta(s + \omega)/2)). \end{aligned} \tag{28}$$

Here, $⨍_{-\infty}^{\infty} ds/s$ denotes the principle value integral, where the $s = 0$ value is excluded from the integration. These definitions allow writing the full Markovian Redfield relaxation tensor in the eigenstate representation, which characterizes the density matrix "transition" rate from ρ_{kl} to ρ_{ij},

$$\begin{aligned}\mathcal{R}_{ijkl} = \sum_n \left(\delta_{jl} M(\omega_{kn})\Lambda_{innk} + \delta_{ki} M^*(\omega_{\ln})\Lambda_{jnnl}\right) \\ - M(\omega_{ki})\Lambda_{iklj} - M^*(\omega_{lj})\Lambda_{ljik},\end{aligned} \tag{29}$$

here $\omega_{kl} = \varepsilon_k - \varepsilon_l$. This expression in the secular approximation reduces to the population relaxation rate matrix between eigenstates, $\Gamma_{kl} = 2\Lambda_{kllk}\Re M(\omega_{kl})$, with the diagonal elements satisfying the detailed balance condition: $\Gamma_{kk} = -\sum_l \Gamma_{lk}$, $l \neq k$. The dephasing rates between any eigenstates are[78]

$$\begin{aligned}\gamma_{ij} = \sum_n \left(M(\omega_{in})\Lambda_{inni} + M^*(\omega_{jn})\Lambda_{jnnj}\right) \\ - 2\Lambda_{iijj}\Re M(0).\end{aligned} \tag{30}$$

The main difference in the present expressions compared to the previous formulation[78] is only technical: the stationary ground state of the system is different from the original ground state in the site basis, and it is involved in the relaxation and decoherence processes. The stationary ground state contains contributions from the molecular excitations, induced by L couplings. This has the effects on relaxation (the excited states decay to the ground state) and on spectra calculations.

Finally, this description aligns with the standard formulation for pigment–protein complexes, wherein the original site basis only molecular transition energies do fluctuate in accord with Eq. (23). Fluctuations of different molecules are not correlated in accord with Eq. (26). The fluctuation spectral densities of all pigments are the same. The spectral content of the environment fluctuations is characterized by the Drude spectral density [in Eq. (27)] with reorganization energy λ of 30 cm^{-1} and timescale γ of 100 cm^{-1},

$$C''(\omega) = 2\lambda \frac{\omega\gamma}{\omega^2 + \gamma^2}. \tag{31}$$

The model corresponds to the exponentially decaying classical correlation function. Of course, all Hamiltonian elements attain fluctuating terms after the transformation to the eigenstate basis [Eq. (26)]; however, the form of the fluctuation spectral densities of all Hamiltonian matrix elements remains conserved as the system–bath coupling is linear. For simplicity and for keeping the theoretical approaches better validated, we do not include the high frequency molecular vibrations. Our main focus of the paper is related to evaluating the non-resonant electronic couplings, which are part of the system Hamiltonian.

There are a lot of different methodologies for how to approach the system–bath coupling; nonetheless, multichromophoric systems pose challenges to the known methodologies as the mixing of the electronic states is present, and it results in off-diagonal elements of exciton–phonon coupling that are hard to determine precisely.[79] Nakajima–Zwanzig[80,81] and Shibata–Takahashi–Hashitsume[82] equations describing the time evolution of quantum mechanical systems are considered to be mathematically exact; however, they are hard to implement for numerical calculations. Therefore, usually the benchmark calculations for multichromophore systems are considered hierarchical equations of motion[83] or stochastic path integral[84] methodologies, although they remain computationally very expensive.

The application of secular or Markovian approximations in the Redfield approach can lead to discrepancies when vibrational degrees of freedom resonate with electronic energy gaps,[85] as in the case of FMO, where electronic couplings and suggested reorganization energies are of the similar magnitude.[86] To reduce the shortcomings of these approximations, methods such as full cumulant expansion have been developed[87] and applied for such systems as LH2.[79] Moreover, such methodologies as the time-dependent Dirac–Frenkel principle[88,89] have been implemented to study J and H molecular aggregates. However, when qualitative evaluation of the dynamics is sufficient, secular Redfield equations are usually utilized, as is the case in the present paper.

C. Absorption spectra

The theoretical background of spectroscopy measurements has been described in detail in Ref. 90. Here, we point to several nuances, which become important when blocks of excited states become not isolated.

The general linear response function of a multilevel system in the dipole approximation is given by

$$S^{(1)}(t) = i\theta(t)\ \mathrm{Tr}\left(\hat{D}\mathcal{G}(t)\mathcal{D}\rho_0\right), \tag{32}$$

where $\hat{D}$ is the dipole operator, $\mathcal{D}\hat{A} = [\hat{D}, \hat{A}]$ is the corresponding dipole superoperator, ρ_0 is the equilibrium density operator, $\theta(t)$ is the Heaviside function, and $\mathcal{G}(t)$ is the density matrix propagator: $\rho(t) = \mathcal{G}(t)\rho(0)$. The electronic ground state is still energetically separated from the other states; hence, the equilibrium density operator implies occupation of the lowest energy state, which we identify by g: $\rho_{eq} = |g\rangle\langle g|$. The full dipole operator in the site-basis in the present case contains transition and permanent dipoles,

$$\hat{D} = \begin{pmatrix} 0 & \boldsymbol{\mu}_1 & \boldsymbol{\mu}_2 & \dots & \boldsymbol{\mu}_N \\ \boldsymbol{\mu}_1 & \Delta\boldsymbol{d}_1 & 0 & \dots & 0 \\ \boldsymbol{\mu}_2 & 0 & \Delta\boldsymbol{d}_2 & \dots & 0 \\ \dots & \dots & \dots & \dots & \dots \\ \boldsymbol{\mu}_N & 0 & 0 & \dots & \Delta\boldsymbol{d}_N \end{pmatrix}, \tag{33}$$

where $\boldsymbol{\mu}_i$ is the transition dipole of the ith chromophore, while $\Delta\boldsymbol{d}_i = \boldsymbol{d}_i^{(e)} - \boldsymbol{d}_i^{(g)}$ is the difference between the permanent dipoles of the excited state and the ground state of the ith chromophore. The permanent dipoles do not contribute to the absorption spectrum when the electronic ground state is isolated in the standard formulation of the Frenkel exciton model. However, when $L \neq 0$, they will contribute to the spectrum due to intermixing with the transition dipoles. Using the Markovian relaxation model and the fact that the ground state is well separated in energy (it is the only state that is populated in equilibrium) in the eigenstate basis, the response function can be explicitly written in the operator matrix elements,

$$S^{(1)}(t) = i\theta(t)\sum_{ikl} \hat{D}_{kl}^{(e)}\mathcal{G}_{kl,ig}(t)\hat{D}_{ig}^{(e)} - c.c. \tag{34}$$

Since the site-basis dipole operator is a sparse matrix, different elements of the dipole operator in the eigenstate basis can be written explicitly,

$$\hat{D}_{ab}^{(e)} = \sum_{i} \left(c_{ga} c_{ib} \boldsymbol{\mu}_i + c_{ia} c_{ib} \Delta \boldsymbol{d}_i \right), \tag{35}$$

where the summation runs only over excited states, while indices a, b involve all states. In the secular approximation, only the diagonal elements of the propagator are included. In the Markovian approximation, only the following elements are relevant for absorption:

$$\mathcal{G}_{eg,eg}(t) = \exp\left(-i\omega_{eg} t - \gamma_{eg} t\right). \tag{36}$$

The absorption spectrum is then given by a Fourier transform of the response function,[78] which yields

$$\kappa(\omega) = \sum_{e} \frac{|\hat{D}_{ge}^{(e)}|^2 \omega_e \Re(\gamma_{ge})}{(\omega_e - \omega_{ge} + \Im(\gamma_{ge}))^2 + \Re(\gamma_{ge})^2}. \tag{37}$$

The transition dipole operator is transformed to the eigenstate representation using the set of system eigenvectors, and the Redfield relaxation matrix is calculated. The absorption spectrum, exciton dephasing, and population relaxation matrices are calculated as well.

These steps are sufficient for the main purpose of the present study, which is about constructing the non-resonant exciton model. The L type couplings become induced by the surrounding proteins. In addition, the inclusion of H_2O molecules would not make a substantial difference because the water molecules are concentrated outside the protein and become quite separated from the pigment molecules. Furthermore, protein equilibration using, e.g., molecular mechanics (MM) methods would lead to fine tuning of the results; however, it would not affect the results qualitatively. Hence, for the present study, the crystallographic information is assumed to be sufficiently accurate.

IV. RESULTS

A. FMO Hamiltonian

The full Hamiltonian of the FMO complex (6MEZ PDB) is presented in Fig. 2, in which intermolecular interactions of S_1, S_2 excited states, their excitation frequencies, and the interaction with a ground state (S_0) are displayed. Intramolecular environment-induced S_1, S_2 interactions are not included, since these are mostly of vibronic origin. The diagonal values of the Hamiltonian represent pigment excitation energy.

The lowest first excitation energy is found for Bchl *a*403 and the highest for *a*406. The lowest energy excitation of the S_2 state is also at *a*403, but the highest is *a*407, as *a*406 excitation is lower by 52 cm^{-1}. The lowest excitation energy agrees with previous studies of Adolphs and Renger[37] and Wendling *et al.*;[36] however, in their work, the highest excitation energy belongs to *a*405, while *a*406 has the second highest energy, but in our work this order is reversed.

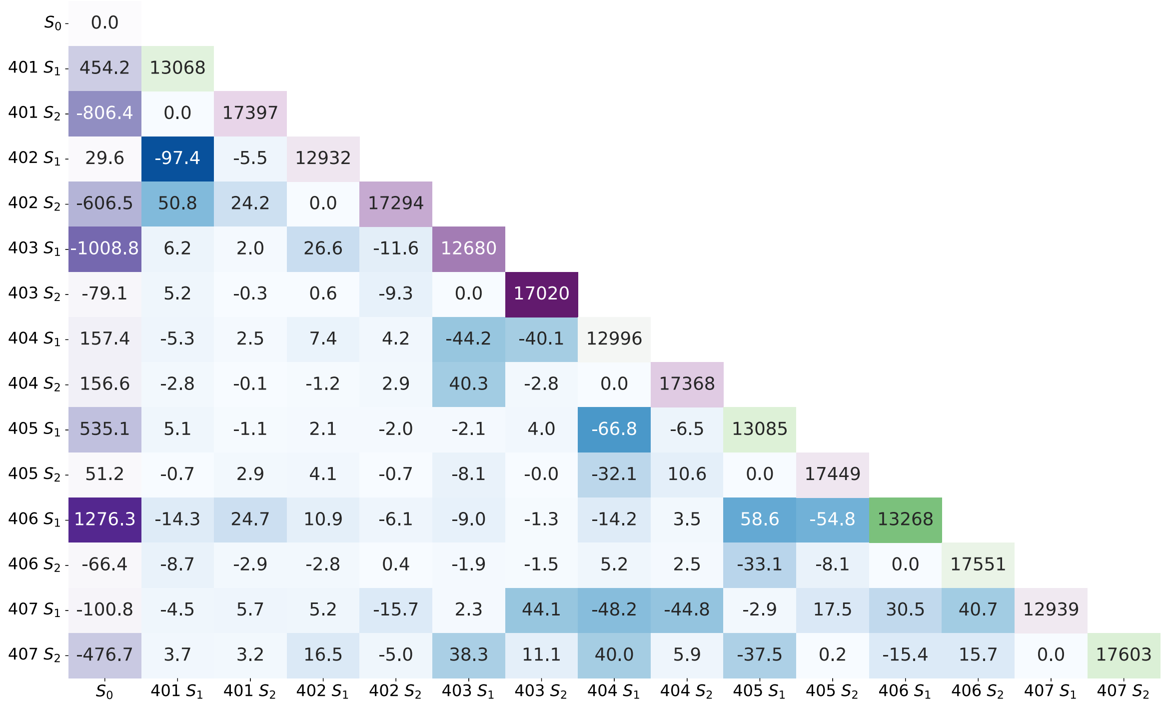

	S_0	401 S_1	401 S_2	402 S_1	402 S_2	403 S_1	403 S_2	404 S_1	404 S_2	405 S_1	405 S_2	406 S_1	406 S_2	407 S_1	407 S_2
S_0	0.0														
401 S_1	454.2	13068													
401 S_2	-806.4	0.0	17397												
402 S_1	29.6	-97.4	-5.5	12932											
402 S_2	-606.5	50.8	24.2	0.0	17294										
403 S_1	-1008.8	6.2	2.0	26.6	-11.6	12680									
403 S_2	-79.1	5.2	-0.3	0.6	-9.3	0.0	17020								
404 S_1	157.4	-5.3	2.5	7.4	4.2	-44.2	-40.1	12996							
404 S_2	156.6	-2.8	-0.1	-1.2	2.9	40.3	-2.8	0.0	17368						
405 S_1	535.1	5.1	-1.1	2.1	-2.0	-2.1	4.0	-66.8	-6.5	13085					
405 S_2	51.2	-0.7	2.9	4.1	-0.7	-8.1	-0.0	-32.1	10.6	0.0	17449				
406 S_1	1276.3	-14.3	24.7	10.9	-6.1	-9.0	-1.3	-14.2	3.5	58.6	-54.8	13268			
406 S_2	-66.4	-8.7	-2.9	-2.8	0.4	-1.9	-1.5	5.2	2.5	-33.1	-8.1	0.0	17551		
407 S_1	-100.8	-4.5	5.7	5.2	-15.7	2.3	44.1	-48.2	-44.8	-2.9	17.5	30.5	40.7	12939	
407 S_2	-476.7	3.7	3.2	16.5	-5.0	38.3	11.1	40.0	5.9	-37.5	0.2	-15.4	15.7	0.0	17603

FIG. 2. Full Hamiltonian (in cm^{-1}) of FMO (6MEZ PDB) using TrEsp methodology from the 6MEZ PDB structure. Excited state inter-pigment interactions are marked in blue, excitation frequencies of the pigments are on the diagonal and marked in green (shift to higher values) or purple (shift to lower values), while interactions with the ground state are presented in the first column and marked in purple.

The strongest resonant interactions between S_1 states are formed between BChl *a* 401–402 (−97 cm^{-1}), 404–405 (−67 cm^{-1}), 405–406 (59 cm^{-1}), 404–407 (−48 cm^{-1}), and 403–404 (−44 cm^{-1}) pairs. All of these pigment pairs have short interchromophore distances between Mg atoms (12.8, 13.9, 11.7, 13.2, and 11.2 Å, respectively). Moreover, these pigment pairs have non-negligible interactions between the first excited and the second excited state: as the charge density in the S_2 state is different from the S_1 state, this impacts the overall magnitude of interaction between different states even when the dipole moment of S_2 is 2.2 times smaller than that of the S_1 state; therefore, it reduces the interaction strength. The absolute values of interactions of S_2 states vary up to 24 cm^{-1}.

In Fig. 3, we present the differences between analyzed models in terms of couplings with the ground state and excitation energy (as the interchromophore interactions remain the same). It is apparent that pigment-induced interaction with the ground state is small, as it results in absolute coupling values varying from 17 cm^{-1} up to 213 cm^{-1}; however, the impact of the protein makes the numbers significantly larger, as the interaction with amino acids can increase the interaction strengths up to ~30 times. There are differences between results obtained by using different FFs: the changes are roughly ~10% for the strongest interactions, except for pigment *a*401 state S_1. The presence of Na^+ ions usually reduces the interaction strength, with notable exceptions being *a*402 S_1, *a*403 S_2, and *a*406 S_2. Figure 3(b) shows that pigment-induced energy shifts are quite small—up to 100 cm^{-1}—and do not represent realistic bacteriochlorophyll environmental splitting. The energy shift patterns become quite similar for both FFs when the protein environment is included: the highest S_1 excitation energy is predicted for the pigment *a*406, while the lowest is for *a*403. However, some small but significant differences occur for the S_1 excitation values positioned in between: *a*401 and *a*402 pigment energies are shifted to higher than average energies, while *a*407 excitation energy is reduced using AMBER FF. The presence of Na^+ ions usually diminishes the excitation energy value, except for pigments *a*402 S_2 and *a*403 S_1 and S_2.

The Hamiltonian matrix obtained for the 3EOJ structure is presented in supplementary material, Figs. S1 and S2. The Hamiltonians calculated with AMBER FF are quite similar between 6MEZ and 3EOJ structures: the largest differences between the strongest inter-pigment interactions occur in the range of 1–3 cm^{-1}. The average absolute difference in excitation energies of the pigments between the two structures is 41 cm^{-1}, but the ordering of the states is exactly the same in both complexes (excluding the additional pigment in the 3EOJ structure). The main differences in excitation energies between the two structures occur in *a*401 and *a*403, which have energy levels that are 60–110 cm^{-1} lower in the 3EOJ structure than in 6MEZ. It is important to note that the additional eighth pigment in the 3EOJ structure has the highest excitation energy of all pigments—as other authors have noted, it may be an energy collector in such a FMO system. Interactions with the ground state are also similar: the deviation between them is 8%–17% across the two structures; nonetheless, the weaker interaction values vary a lot more.

Regarding the off-resonant coupling to the S_0 state, we find that these coupling amplitudes and the overall coupling pattern are quite scattered—Bchl *a*403 S_1 and *a*406 have the largest magnitude of interactions (differing by the sign); however, in some cases, the S_2 interaction with the ground state is larger than the S_1 interaction with it (BChl *a*401, *a*402, *a*407). The scale of interaction varies mainly from 10^2 to 10^3; therefore, it is obvious that these terms are

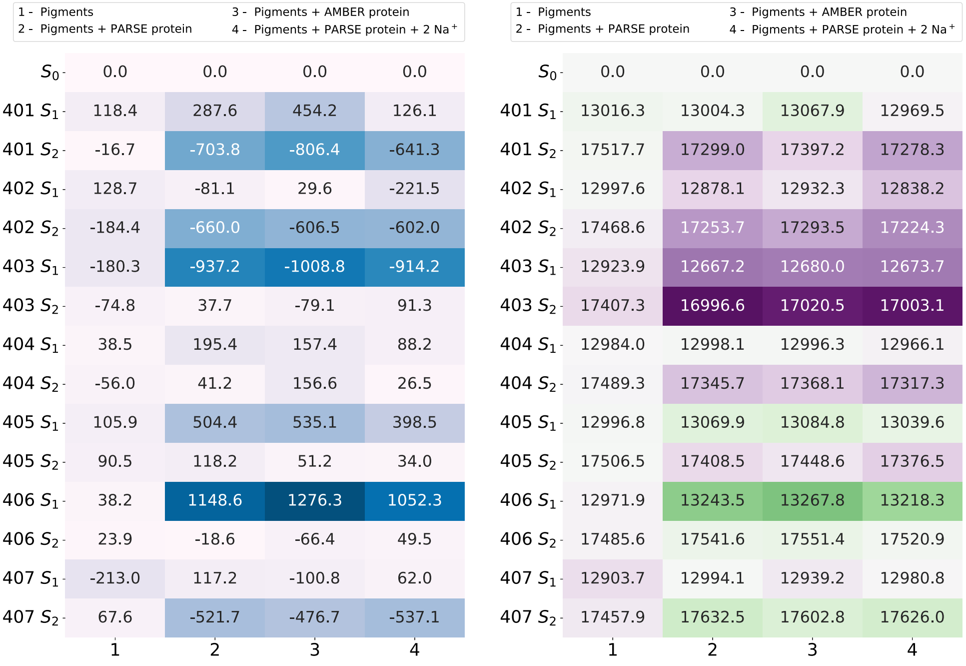

1 - Pigments
2 - Pigments + PARSE protein
3 - Pigments + AMBER protein
4 - Pigments + PARSE protein + 2 Na^+

	1	2	3	4
S_0	0.0	0.0	0.0	0.0
401 S_1	118.4	287.6	454.2	126.1
401 S_2	-16.7	-703.8	-806.4	-641.3
402 S_1	128.7	-81.1	29.6	-221.5
402 S_2	-184.4	-660.0	-606.5	-602.0
403 S_1	-180.3	-937.2	-1008.8	-914.2
403 S_2	-74.8	37.7	-79.1	91.3
404 S_1	38.5	195.4	157.4	88.2
404 S_2	-56.0	41.2	156.6	26.5
405 S_1	105.9	504.4	535.1	398.5
405 S_2	90.5	118.2	51.2	34.0
406 S_1	38.2	1148.6	1276.3	1052.3
406 S_2	23.9	-18.6	-66.4	49.5
407 S_1	-213.0	117.2	-100.8	62.0
407 S_2	67.6	-521.7	-476.7	-537.1

(a)

1 - Pigments
2 - Pigments + PARSE protein
3 - Pigments + AMBER protein
4 - Pigments + PARSE protein + 2 Na^+

	1	2	3	4
S_0	0.0	0.0	0.0	0.0
401 S_1	13016.3	13004.3	13067.9	12969.5
401 S_2	17517.7	17299.0	17397.2	17278.3
402 S_1	12997.6	12878.1	12932.3	12838.2
402 S_2	17468.6	17253.7	17293.5	17224.3
403 S_1	12923.9	12667.2	12680.0	12673.7
403 S_2	17407.3	16996.6	17020.5	17003.1
404 S_1	12984.0	12998.1	12996.3	12966.1
404 S_2	17489.3	17345.7	17368.1	17317.3
405 S_1	12996.8	13069.9	13084.8	13039.6
405 S_2	17506.5	17408.5	17448.6	17376.5
406 S_1	12971.9	13243.5	13267.8	13218.3
406 S_2	17485.6	17541.6	17551.4	17520.9
407 S_1	12903.7	12994.1	12939.2	12980.8
407 S_2	17457.9	17632.5	17602.8	17626.0

(b)

FIG. 3. Comparison of properties (in cm^{-1}) of 6MEZ FMO Hamiltonians in various models: (a) coupling to the ground state and (b) excitation energy.

not negligible and should be considered when describing excitation resonances and exciton time evolution.

B. FMO energy relaxation

The full set of off-diagonal coupling elements in the Hamiltonian leads to exciton intra-band and inter-band energy relaxation. Figure 4 represents transfer times between various states at 77 K. It is apparent that the two excitation transfer blocks are formed—one for the S_1 states (states 2–8) and the other for the S_2 excited states (states 9–15). Inside the S_1 excitation block, we see that the fastest transfer times are hundreds of femtoseconds long and usually occur between excited states that are similar in energy. 0.3 ps transfer happens from state 6 to 5, which both are composed of excitations on pigments *a*404 and *a*405 (57% *a*405 + 29% *a*404 and 41% *a*404 + 23% *a*405 + 29% *a*407). Another 0.3 ps transfer occurs from state 5 to 4, which is composed of excitations on *a*407 and *a*404. Moreover, it is apparent that state no. 2 in the transfer table, which comprises 90% excitation on the lowest energy pigment *a*403, usually receives population transfer to this state in the range of several dozen picoseconds; however, it is slow to transfer its population to the states with higher excitation energies, therefore acting as a sink in the FMO complex. A different situation can be seen for the highest energy S_1 excited state 8 (85% *a*406), which mostly delivers excitation to the other states as the population transfers toward that particular state very slowly.

An interesting phenomenon can be seen in the S_2 excitation block—despite the fact that most of the transfer times are slower than transfer times between S_1 states, the 100 fs relaxation channel exists between states 12 ↔ 13. States 12 and 13 are composed of pigments *a*401 and *a*405. The near picosecond long transfer times occur in the direction of excitations 15 → 14 (0.8 ps, 92% *a*407 → 94% *a*406) and 13 → 10 (1.1 ps, 53% *a*401 + 34% *a*405 → 87% *a*402), which have significant magnitudes of interaction strengths in the Hamiltonian.

Next, we consider the inter-block relaxation. The lifetimes of the most excitons vary in the range from hundreds of femtoseconds up to several picoseconds, but the lowest energy S_1 and S_2 excitations (states 2 and 9) have longer lifetimes as they are emitting energy out of the complex and usually not transferring it to any nearby BChls. The transfer times from excited states to the ground state mostly vary from several to tens of nanoseconds—the two shortest times are for second and eighth states, where excitons are localized 90% on *a*403 and 85% on *a*406 pigments, respectively, and they have the strongest interactions with the ground state in the Hamiltonian, while the slowest times can be observed for the third and fourth states, which are mainly localized on pigments *a*402 (76%) and *a*407 (67%) and have small interaction energies with the ground state. Relaxation from the S_2 state to the S_0 state is a bit slower—occurring in the interval from 10 to 700 ns. The fastest relaxation channels in the direction $S_2 \to S_0$ are those that have strong S_2–S_0 couplings in the Hamiltonian; therefore, states 10 (87% *a*402 + 12% *a*401) and 13 (53% *a*401 + 34% *a*405) have a relaxation time of ~10 ns. Similarly, according to our model, population relaxation in the $S_2 \to S_1$ direction varies in the order of 10^4–10^5 ps. Finally, the energy transfer from the ground state to the excited states and from the S_1 block to the S_2 block requires a large activation energy; therefore, such an up-hill transfer time is infinitely long.

C. FMO absorption

The Hamiltonian matrix allows direct calculation of the simplest experimental observable—the optical absorption spectrum. The calculated absorption spectra of the FMO complex are shown in

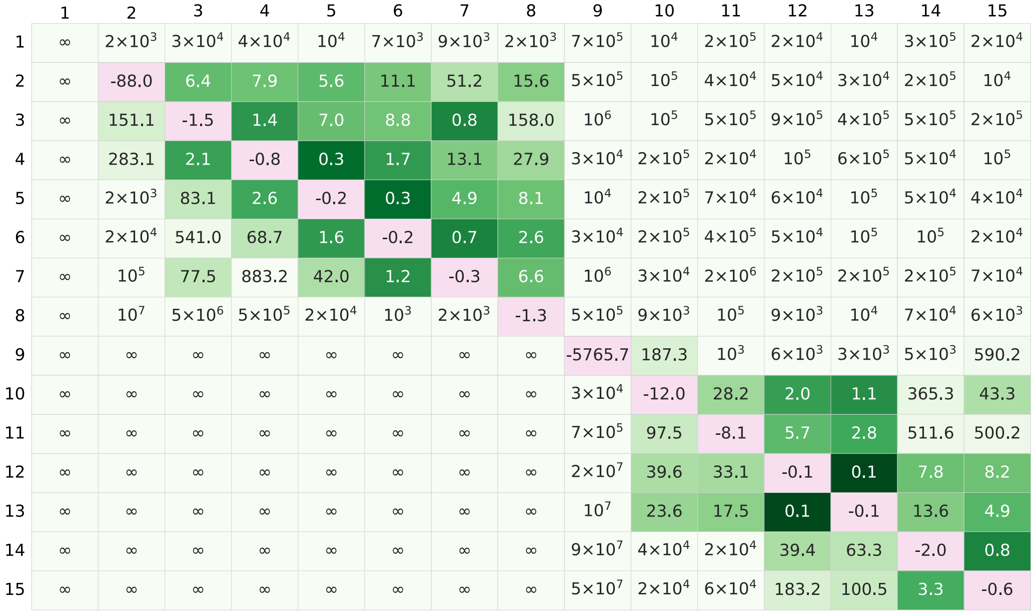

	1	2	3	4	5	6	7	8	9	10	11	12	13	14	15
1	∞	2×10^{3}	3×10^{4}	4×10^{4}	10^{4}	7×10^{3}	9×10^{3}	2×10^{3}	7×10^{5}	10^{4}	2×10^{5}	2×10^{4}	10^{4}	3×10^{5}	2×10^{4}
2	∞	-88.0	6.4	7.9	5.6	11.1	51.2	15.6	5×10^{5}	10^{5}	4×10^{4}	5×10^{4}	3×10^{4}	2×10^{5}	10^{4}
3	∞	151.1	-1.5	1.4	7.0	8.8	0.8	158.0	10^{6}	10^{5}	5×10^{5}	9×10^{5}	4×10^{5}	5×10^{5}	2×10^{5}
4	∞	283.1	2.1	-0.8	0.3	1.7	13.1	27.9	3×10^{4}	2×10^{5}	2×10^{4}	10^{5}	6×10^{5}	5×10^{4}	10^{5}
5	∞	2×10^{3}	83.1	2.6	-0.2	0.3	4.9	8.1	10^{4}	2×10^{5}	7×10^{4}	6×10^{4}	10^{5}	5×10^{4}	4×10^{4}
6	∞	2×10^{4}	541.0	68.7	1.6	-0.2	0.7	2.6	3×10^{4}	2×10^{5}	4×10^{5}	5×10^{4}	10^{5}	10^{5}	2×10^{4}
7	∞	10^{5}	77.5	883.2	42.0	1.2	-0.3	6.6	10^{6}	3×10^{4}	2×10^{6}	2×10^{5}	2×10^{5}	2×10^{5}	7×10^{4}
8	∞	10^{7}	5×10^{6}	5×10^{5}	2×10^{4}	10^{3}	2×10^{3}	-1.3	5×10^{5}	9×10^{3}	10^{5}	9×10^{3}	10^{4}	7×10^{4}	6×10^{3}
9	∞	∞	∞	∞	∞	∞	∞	∞	-5765.7	187.3	10^{3}	6×10^{3}	3×10^{3}	5×10^{3}	590.2
10	∞	∞	∞	∞	∞	∞	∞	∞	3×10^{4}	-12.0	28.2	2.0	1.1	365.3	43.3
11	∞	∞	∞	∞	∞	∞	∞	∞	7×10^{5}	97.5	-8.1	5.7	2.8	511.6	500.2
12	∞	∞	∞	∞	∞	∞	∞	∞	2×10^{7}	39.6	33.1	-0.1	0.1	7.8	8.2
13	∞	∞	∞	∞	∞	∞	∞	∞	10^{7}	23.6	17.5	0.1	-0.1	13.6	4.9
14	∞	∞	∞	∞	∞	∞	∞	∞	9×10^{7}	4×10^{4}	2×10^{4}	39.4	63.3	-2.0	0.8
15	∞	∞	∞	∞	∞	∞	∞	∞	5×10^{7}	2×10^{4}	6×10^{4}	183.2	100.5	3.3	-0.6

FIG. 4. Transfer times (in ps) between eigenstates at 77 K in FMO from the 6MEZ PDB structure. The diagonal elements represent net excitation lifetimes.

Figs. 5 and 6 using different levels of modeling. Spectra mapped onto each other are present in supplementary material Fig. S5. For comparison, we present results using the full model vs the block-diagonal model with off-resonant couplings deleted, $L = 0$.

Starting with the block-diagonal model spectra, where L type couplings are ignored, we can see that the FMO pigment-only absorption band is quite narrow and shows three distinct peaks in the Q_y excitation region (12 855, 12 945, and 13 130 cm^{-1}) and only one peak in the Q_x region (17 450 cm^{-1}). Here, we can already see that the Q_x region is of significantly lower intensity than Q_y, as its transition dipole moment is smaller. When we incorporate the protein environment, the surroundings of the BChls change drastically—as different BChls experience the influence of different amino acids, which is apparent in absorption spectra. Comparing FMO pigment-only to pigment + PARSE protein spectra, the spectrum becomes much broader with clearly pronounced five peaks in the Q_y region. Consider the FMO 6MEZ spectrum structure: the first peak of ~0.2 intensity appears at 12 650 cm^{-1}, a medium intensity at ~12 850 cm^{-1}, the highest intensity at ~12 925 cm^{-1}, followed by another medium intensity peak at ~13 050 cm^{-1} and low intensity at ~13 275 cm^{-1}. Ion impact is not significant in FMO 6MEZ spectra as the overall spectra structure looks similar, but medium intensity peak absorption decreases around 5% in absorption value and shifts by 15–20 cm^{-1} to the right, while the leftmost peak shifts around 25 cm^{-1} to the left in both Q_x and Q_y bands. However, the spectrum shape differs with AMBER FF—the highest intensity peak follows the leftmost low intensity peak at ~12 900 cm^{-1}, then comes about 2.5 times lower intensity peak in the middle at 13 000 cm^{-1} and a peak of ~0.6 intensity at 13 100 cm^{-1}, which resembles the experimental spectra shape quite well.[36]

For comparison, we also present results for the 3EOJ structure, whose Hamiltonian is presented in the supplementary material. It is important to note that the 3EOJ PDB structure has 8 bacteriochlorophylls instead of 7. Comparing the absorption spectrum of 6MEZ to the 3EOJ structure, the overall appearance of each type of spectrum is quite similar. However, the main difference between the pigment-only spectra is that FMO 6MEZ has a more pronounced shoulder at 13 025 cm^{-1} and 0.06 higher intensity of a band at 12 855 cm^{-1}, while the Q_x peak has a slightly bigger intensity in the 3EOJ structure at 17 475–17 550 cm^{-1}. The main differences between 6MEZ and 3EOJ PARSE spectra are that 3EOJ has two distinct peaks in the Q_y region 13 000–13 200 cm^{-1}, while 6MEZ has a single peak, and an additional peak at ~13 550 cm^{-1}. In both structures, PARSE FF leads to five distinct peaks in the Q_x spectral region—one separated at 17 000 cm^{-1} and the main band lying between 17 200 and 17 600 cm^{-1} in the 6MEZ structure. However, 3EOJ has a bit higher intensity in the range between 17 400 and 17 600 cm^{-1}. When comparing the AMBER spectra of the 6MEZ and 3EOJ structures, the 6MEZ structure shows higher intensity in the middle and second-highest peaks in the Q_y band, which is also narrower than in the 3EOJ case, while low intensity peaks are closer to the high intensity ones by ~50 cm^{-1}. A similar tendency is present in the Q_x band as well: the lowest energy peak is closer to the main block of excitations, and the two most prominent peaks in the range 17 200–17 600 cm^{-1}

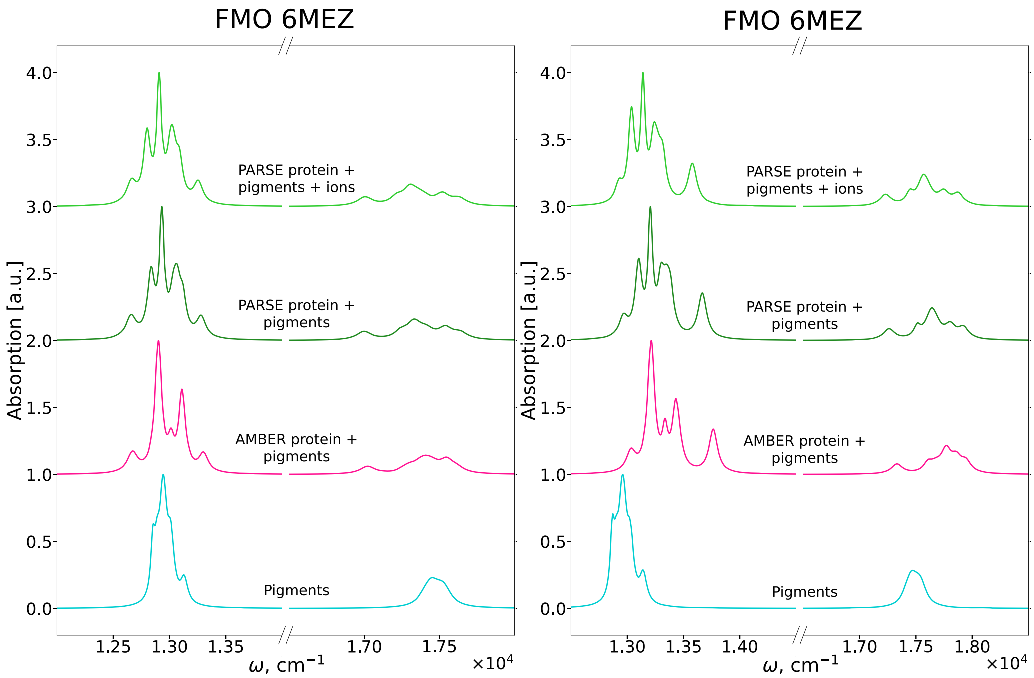

(a) (b)

FIG. 5. Absorption spectra of FMO 6MEZ at 77 K calculated using the secular approximation of Redfield equation solutions: (a) block-diagonal model and (b) full model.

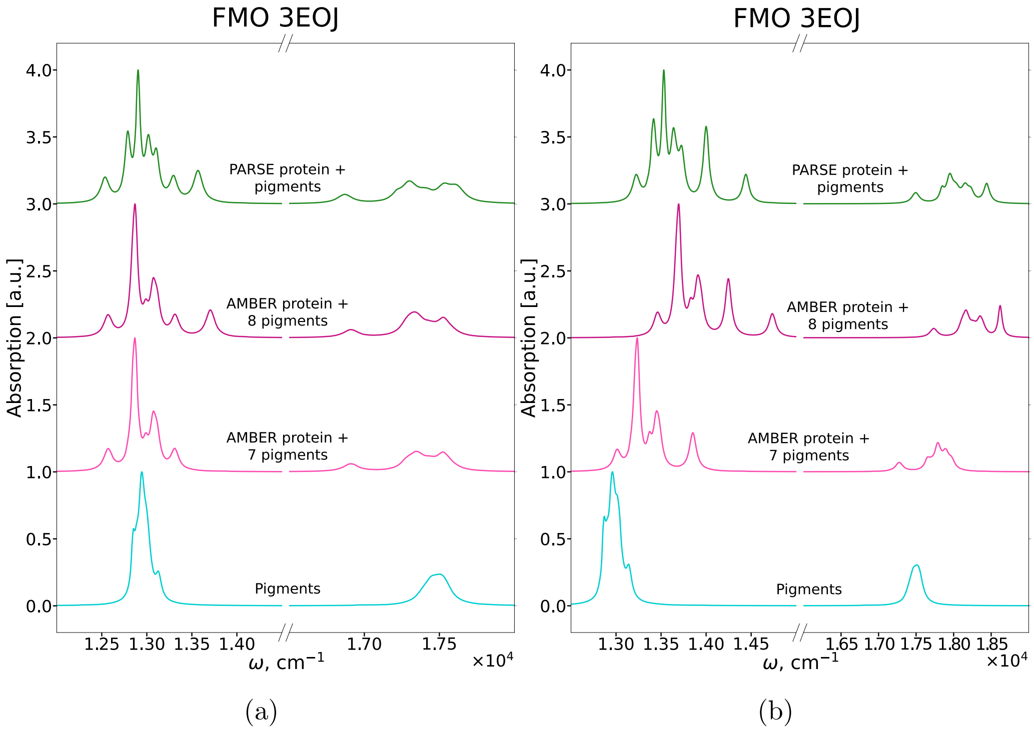

(a) (b)

FIG. 6. Absorption spectra of the FMO 3EOJ PDB structure at 77 K calculated using the secular approximation of Redfield equation solutions: (a) block-diagonal model and (b) full model.

are closer to each other in 6MEZ than in 3EOJ. However, adding the eighth pigment in the 3EOJ structure does not change the absorption of the main band at all but just results in an additional peak at 13 700 cm^{-1}, and in the Q_x region, a slight increase in intensity is seen in the range from 17 200 to 17 400 cm^{-1}.

Next, we focus on the full model with non-resonant L type couplings included. In the pigment-only spectrum, the L-type terms increase the absorption intensity of the peaks on the sides in the Q_y band, while the Q_x band remains homogeneous but also becomes of higher intensity. Comparing Figs. 5 and 6, it is clear that when the protein environment is included, there is a shift of spectra toward higher energies. Nevertheless, not only the spectral position changes, but the overall appearance of the absorption spectrum change. First, the low energy peaks shift to higher energies and merge with the main Q_y band. Second, using PARSE FF, the two peaks of higher energy in the 3EOJ structure, or one peak in the 6MEZ structure, significantly increase in intensity and separate from the core of the Q_y band by 125 cm^{-1} compared to the $L = 0$ case, while the second leftmost peak slightly increases in intensity. ∼13 050 cm^{-1} peak in the full model becomes a bit wider and splits into two in the 13 300–13 400 cm^{-1} region. In the Q_x region, the highest absorption value increases around 1.5 times, and peaks become more pronounced. Similar tendencies can be seen in spectra generated with AMBER FF; however, in the 6MEZ structure, the peak in the middle becomes more intense, and the 13 100 cm^{-1} peak slightly decreases, and they both shift by 25 cm^{-1} to the right if we align the positions of FMO absorption spectrum maximum values. The rightmost peak in the Q_y band shift is even more drastic with AMBER than PARSE—by 150 cm^{-1}. Q_x band experiences similar tendencies using both FFs, as in general the absorption in that region increases and peaks become more pronounced. However, the presence of the eighth pigment creates an additional absorption band in the 3EOJ structure's Q_x region at 18 620 cm^{-1}, while its absorption in Q_y is slightly reduced.

D. Fucoxanthin–chlorophyll protein complex

The FMO complex consists of BChl pigments where S_1 and S_2 excited states are spectrally well separated. These states are much less separated in chlorophylls. The inter-state mixing thus becomes much more significant, and excitation properties are more complex in chlorophyll aggregates. FCP complex is a small chlorophyll complex, where the details of the couplings are not overwhelmed by complex inhomogeneities.

The full Hamiltonian of FCP was calculated using the same principles as FMO as described earlier. The resulting Hamiltonian is presented in Fig. 7. Most importantly, S_1–S_0 coupling terms in FCP are non-negligible as well—their values vary from a few reciprocal centimeters up to almost 10^3 cm^{-1}. The strongest interactions are for the pigments a406 (−805 cm^{-1}) and a407 (977 cm^{-1}). S_2 states are also strongly coupled with the ground state. Notice that there are cases where S_2 states interact more strongly with the S_0 state than with S_1 states (a402, a405, $c_1$408, $c_2$403). The lowest energy excited state S_1 belongs to pigment a407 (14 924 cm^{-1}), while the largest downward energy shift occurs in Chls c_1 and c_2. Similar tendencies are also observed in the S_2 excited states. Resonant

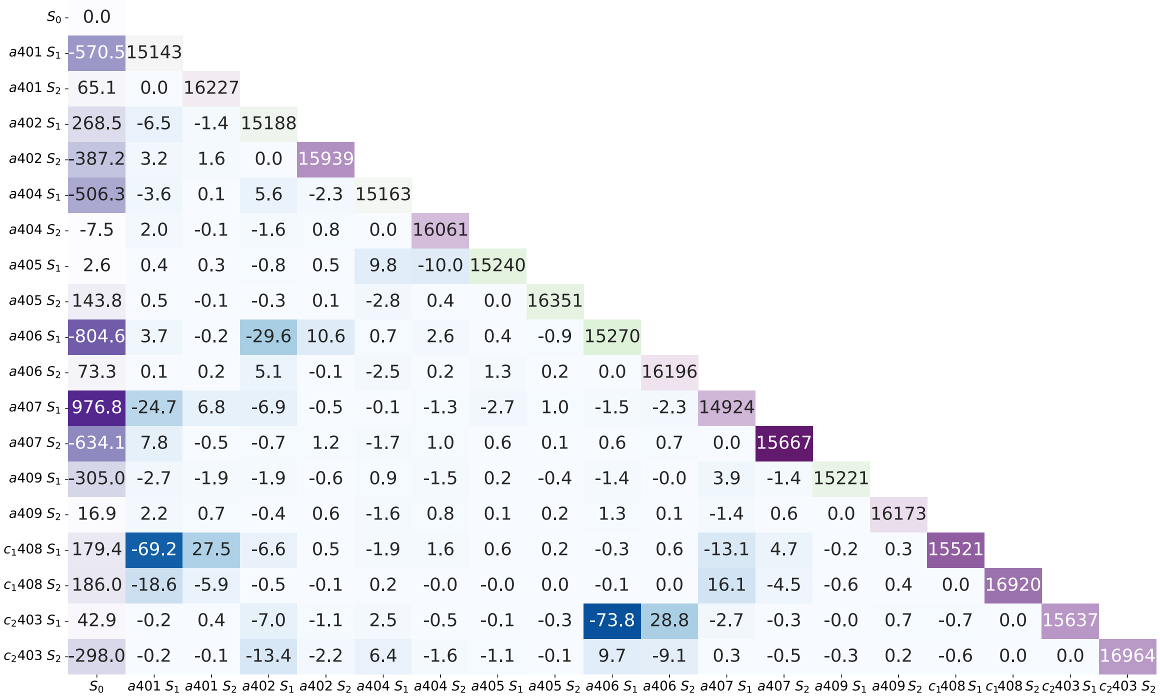

	S_0	a401 S_1	a401 S_2	a402 S_1	a402 S_2	a404 S_1	a404 S_2	a405 S_1	a405 S_2	a406 S_1	a406 S_2	a407 S_1	a407 S_2	a409 S_1	a409 S_2	$c_1$408 S_1	$c_1$408 S_2	$c_2$403 S_1	$c_2$403 S_2
S_0	0.0																		
a401 S_1	-570.5	15143																	
a401 S_2	65.1	0.0	16227																
a402 S_1	268.5	-6.5	-1.4	15188															
a402 S_2	-387.2	3.2	1.6	0.0	15939														
a404 S_1	-506.3	-3.6	0.1	5.6	-2.3	15163													
a404 S_2	-7.5	2.0	-0.1	-1.6	0.8	0.0	16061												
a405 S_1	2.6	0.4	0.3	-0.8	0.5	9.8	-10.0	15240											
a405 S_2	143.8	0.5	-0.1	-0.3	0.1	-2.8	0.4	0.0	16351										
a406 S_1	-804.6	3.7	-0.2	-29.6	10.6	0.7	2.6	0.4	-0.9	15270									
a406 S_2	73.3	0.1	0.2	5.1	-0.1	-2.5	0.2	1.3	0.2	0.0	16196								
a407 S_1	976.8	-24.7	6.8	-6.9	-0.5	-0.1	-1.3	-2.7	1.0	-1.5	-2.3	14924							
a407 S_2	-634.1	7.8	-0.5	-0.7	1.2	-1.7	1.0	0.6	0.1	0.6	0.7	0.0	15667						
a409 S_1	-305.0	-2.7	-1.9	-1.9	-0.6	0.9	-1.5	0.2	-0.4	-1.4	-0.0	3.9	-1.4	15221					
a409 S_2	16.9	2.2	0.7	-0.4	0.6	-1.6	0.8	0.1	0.2	1.3	0.1	-1.4	0.6	0.0	16173				
$c_1$408 S_1	179.4	-69.2	27.5	-6.6	0.5	-1.9	1.6	0.6	0.2	-0.3	0.6	-13.1	4.7	-0.2	0.3	15521			
$c_1$408 S_2	186.0	-18.6	-5.9	-0.5	-0.1	0.2	-0.0	-0.0	0.0	-0.1	0.0	16.1	-4.5	-0.6	0.4	0.0	16920		
$c_2$403 S_1	42.9	-0.2	0.4	-7.0	-1.1	2.5	-0.5	-0.1	-0.3	-73.8	28.8	-2.7	-0.3	-0.0	0.7	-0.7	0.0	15637	
$c_2$403 S_2	-298.0	-0.2	-0.1	-13.4	-2.2	6.4	-1.6	-1.1	-0.1	9.7	-9.1	0.3	-0.5	-0.3	0.2	-0.6	0.0	0.0	16964

FIG. 7. Full Hamiltonian (in cm^{-1}) of FCP using the TrEsp methodology from the 6A2W PDB structure.

couplings between excited states reflect the previous study,[68] while the absolute coupling values between S_1 and S_2 states vary from 10 to 29 cm^{-1}.

Figure 8 shows the transfer times between FCP eigenstates. In this model, the lowest energy excitation is primarily localized on Chl *a*407 (90%), which acts as the main sink of populations. The fastest transfer occurs for states 3–5. These states are delocalized (especially state 4, which has 12%–37% 401, 402, 404, and 406). It is apparent that states 6 and 7 are relatively slower at transferring their excitation energy to other states—they are mainly localized on pigments *a*409 and *a*405, which have weak interactions with other pigments and are quite distant spatially from them. Quite a fast

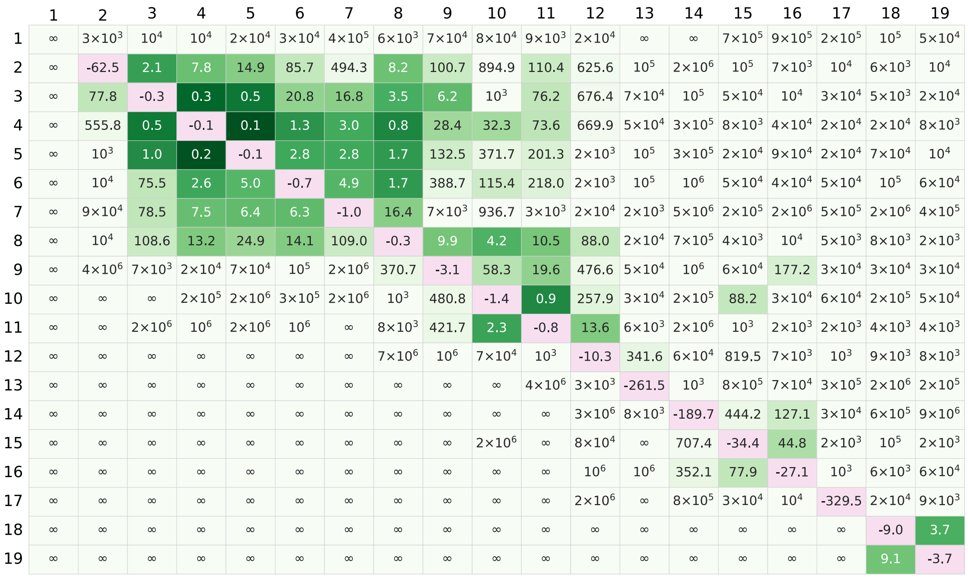

	1	2	3	4	5	6	7	8	9	10	11	12	13	14	15	16	17	18	19
1	∞	3×10^3	10^4	10^4	2×10^4	3×10^4	4×10^5	6×10^3	7×10^4	8×10^4	9×10^3	2×10^4	∞	∞	7×10^5	9×10^5	2×10^5	10^5	5×10^4
2	∞	-62.5	2.1	7.8	14.9	85.7	494.3	8.2	100.7	894.9	110.4	625.6	10^5	2×10^6	10^5	7×10^3	10^4	6×10^3	10^4
3	∞	77.8	-0.3	0.3	0.5	20.8	16.8	3.5	6.2	10^3	76.2	676.4	7×10^4	10^5	5×10^4	10^4	3×10^4	5×10^3	2×10^4
4	∞	555.8	0.5	-0.1	0.1	1.3	3.0	0.8	28.4	32.3	73.6	669.9	5×10^4	3×10^5	8×10^3	4×10^4	2×10^4	2×10^4	8×10^3
5	∞	10^3	1.0	0.2	-0.1	2.8	2.8	1.7	132.5	371.7	201.3	2×10^3	10^5	3×10^5	2×10^4	9×10^4	2×10^4	7×10^4	10^4
6	∞	10^4	75.5	2.6	5.0	-0.7	4.9	1.7	388.7	115.4	218.0	2×10^3	10^5	10^6	5×10^4	4×10^4	5×10^4	10^5	6×10^4
7	∞	9×10^4	78.5	7.5	6.4	6.3	-1.0	16.4	7×10^3	936.7	3×10^3	2×10^4	2×10^3	5×10^6	2×10^5	2×10^6	5×10^5	2×10^6	4×10^5
8	∞	10^4	108.6	13.2	24.9	14.1	109.0	-0.3	9.9	4.2	10.5	88.0	2×10^4	7×10^5	4×10^3	10^4	5×10^3	8×10^3	2×10^3
9	∞	4×10^6	7×10^3	2×10^4	7×10^4	10^5	2×10^6	370.7	-3.1	58.3	19.6	476.6	5×10^4	10^6	6×10^4	177.2	3×10^4	3×10^4	3×10^4
10	∞	∞	∞	2×10^5	2×10^6	3×10^5	2×10^6	10^3	480.8	-1.4	0.9	257.9	3×10^4	2×10^5	88.2	3×10^4	6×10^4	2×10^5	5×10^4
11	∞	∞	2×10^6	10^6	2×10^6	10^6	∞	8×10^3	421.7	2.3	-0.8	13.6	6×10^3	2×10^6	10^3	2×10^3	2×10^3	4×10^3	4×10^3
12	∞	∞	∞	∞	∞	∞	∞	7×10^6	10^6	7×10^4	10^3	-10.3	341.6	6×10^4	819.5	7×10^3	10^3	9×10^3	8×10^3
13	∞	∞	∞	∞	∞	∞	∞	∞	∞	∞	4×10^6	3×10^3	-261.5	10^3	8×10^5	7×10^4	3×10^5	2×10^6	2×10^5
14	∞	∞	∞	∞	∞	∞	∞	∞	∞	∞	∞	3×10^6	8×10^3	-189.7	444.2	127.1	3×10^4	6×10^5	9×10^6
15	∞	∞	∞	∞	∞	∞	∞	∞	∞	2×10^6	∞	8×10^4	∞	707.4	-34.4	44.8	2×10^3	10^5	2×10^3
16	∞	∞	∞	∞	∞	∞	∞	∞	∞	∞	∞	10^6	10^6	352.1	77.9	-27.1	10^3	6×10^3	6×10^4
17	∞	∞	∞	∞	∞	∞	∞	∞	∞	∞	∞	2×10^6	∞	8×10^5	3×10^4	10^4	-329.5	2×10^4	9×10^3
18	∞	∞	∞	∞	∞	∞	∞	∞	∞	∞	∞	∞	∞	∞	∞	∞	∞	-9.0	3.7
19	∞	∞	∞	∞	∞	∞	∞	∞	∞	∞	∞	∞	∞	∞	∞	∞	∞	9.1	-3.7

FIG. 8. Transfer times (in ps) between excited states at 77 K in FCP from the 6A2W PDB structure. The transfer times larger than 10^7 ps were marked as ∞.

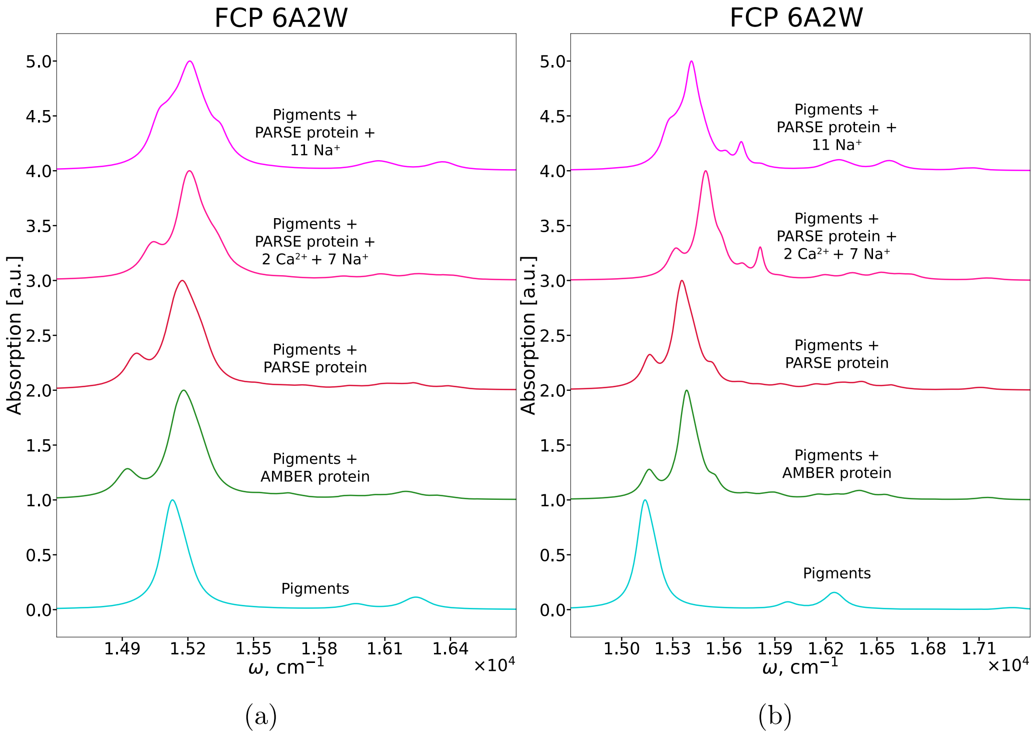

(a) (b)

FIG. 9. Absorption spectra of FCP at 77 K using (a) block-diagonal model and (b) full model Hamiltonian.

transfer is also possible between Chl *c* and Chl *a*: there are 6 and 4 ps transfers between states 9 → 3 and 10 → 8 (mainly pigments $c_1$408 → a401 and $c_2$403 → a406, respectively). However, the most interesting result is the transfer between states 10 and 11—excitations of these states are localized almost solely on $c_2$403 S_1 and a407 S_2. The excitation frequencies of these states are almost identical; therefore, there is a population transfer channel in both directions. It is interesting to note that Chl c_2 S_1 excitation has 4% character of S_2 a407 excitation, which is not the case in FMO. Overall, the relaxation $S_2 \rightarrow S_1$ between most of the pigments happens between 10 and 1000 ns. Moreover, our model shows that the upward transfer $S_1 \rightarrow S_2$ between other Chls is also possible in FCP, but occurs as a very slow process (usually $>10^7$ ps).

Finally, the calculated absorption spectra of FCP are presented in Fig. 9. When protein is excluded, all Chl *a* Q_y excitations appear like a single peak around 15 150 cm^{-1}, followed by weaker peaks (around 0.1 a.u.) of Chl c_1 and $c_2 Q_y$ excitations ∼15 960 cm^{-1} and Chl *a* Q_x excitations at 16 240 cm^{-1}. Chls *c* Q_x excitations are very weak, present at ∼17 270 cm^{-1}, and their absorption intensity is only around 0.01 a.u. Adding the protein environment induces reshaping of the main Q_y Chl *a* peak, which is no longer a single peak in that region—a shoulder peak at 250 cm^{-1} (PARSE FF) before the main peak appears, and the Chl *a* Q_x and Chl *c* Q_y excitations spread out between 15 400 and 16 400 cm^{-1} and form multiple peaks due to the different environment they are experiencing. The main difference between the PARSE and AMBER FF is that the leftmost peak is shifted to the left by 50 cm^{-1}, and the 15 400–16 400 cm^{-1} absorption range has slightly different peak positions and absorption values. When Na$^+$ ions are added to neutralize the system, the Chl *a* Q_y excitation region becomes more homogeneous, similar to its experimental structure, while the Q_x excitation of Chl *a* and the first excitation of Chl *c* stay as two more pronounced peaks. Chl *c* Q_x excitations are almost negligible, with very low intensity, as the second excited state dipole moment of Chl *c* is significantly smaller than the first one. The main changes in the spectra that are caused by adding the non-resonant *L*-terms are (1) the spectra shift to higher frequencies, (2) the spectra become narrower in the Chl *a* Q_y zone, the shoulder peak position and intensity varies, and the higher frequency Q_y excitation forms a bump near the main band or separates completely, and (3) the intensities of the higher energy Chl *a* Q_x and Chl *c* Q_y, Q_x excitations increase.

V. DISCUSSION

The commonly accepted exciton model is constructed as an isolated block of excited states. Such a model includes exciton delocalization and exciton relaxation inside the block and demonstrates a unique absorption spectrum depending on the inter-chromophore coupling pattern. Multi-exciton properties determine the non-linear exciton spectra. However, the exciton number is always conserved, i.e., the exciton lifetime is infinite.

In the present study, we denote such a model as the resonant exciton model. Such a model (being convenient) is approximate.

The above-mentioned blocks are not isolated, and the full Hamiltonian matrix in general does not split into isolated blocks. We have calculated all inter-block matrix elements from structural data. The calculations involve the same chromophore parameters as used in the resonant model. As the inter-chromophore coupling pattern and chromophore energy shifts are well supported by previous studies, the non-resonant coupling amplitudes use the same input parameters and are accurate. The calculated values turn out to be much larger than inter-chromophore resonant couplings. While they are between states that are separated by optical energy gaps, they must certainly contribute to exciton dynamics and optical spectra by affecting the overall energy landscape.

The environment-induced non-resonant couplings result from cumulative electrostatic effects of the surrounding molecules (in their corresponding ground states) interacting with the transition charge density of the pigment molecules. As such, the non-resonant couplings depend very much on the charge distribution in the environment: if the environment is homogeneous (e.g., in an ideal solvent of small molecules), then the cumulative interactions could average to zero due to homogeneity. However, that is not the case for pigment–protein aggregates, where the proteins pose very heterogeneous environmental conditions with strong local electric fields, so the cumulative couplings turn out to be appreciable.

The term non-adiabatic is typically used to describe the coupling between different electronic states induced by nuclear vibrational motion. These types of couplings are necessary to understand more complex transitions between excited states and, most importantly, to describe the processes near conical intersections. However, these are the only degrees of freedom, which couple adiabatic electronic surfaces in isolated molecules. In our work, we consider environment-induced couplings between electronic states. The approach is completely valid for separate molecules in solution as well, and it could be considered as another type of non-adiabaticity when the ground state of a molecule becomes coupled to its excited state due to electrostatic interaction with the environment, e.g., the protein in our case. To discriminate from the vibration-induced non-adiabatic effects, we denote the environment-induced non-adiabaticity by the term non-resonant coupling.

Because of non-resonant couplings, the exciton number becomes not conserved—the excitons have a finite lifetime, which is of the order of nanoseconds. Much larger is the contribution to spectral properties. First, the exciton energies shift to higher energy levels. These shifts of excitons are not uniform; hence, the absorption shape becomes affected. As a result, the exciton models, which have been fitted to various experiments, must be revisited to update the parameters. Second, the permanent dipole moments of the chromophores in their ground or excited states become involved in transition amplitudes for excitons. Therefore, even if excitation amplitudes of some chromophoric states may be small, the large permanent dipoles may contribute to the opening of excitation in optical spectra. This may be a small contribution for FMO; however, complexes with charge transfer (CT) states may be considerably affected, as this introduces an additional mechanism that enables the excitation of CT states directly.

The FMO complex is one of the simplest pigment–protein complexes: BChls have very weak expression of molecular vibrations, and there are no additional types of pigments. β-sheets in FMO comprise most of its protein structure, while α-helices and random coils are primarily in the contact region between subunits.[91] All BChls are hidden in a "pocket" of proteins—the protein does not intervene between different BChls, affecting each BChl only from one side. Moreover, it is not highly charged; therefore, the compensation with charges does not affect the spectra. Therefore, it is almost an ideal structure for modeling novel parameters in pigment–protein complexes, and the electrostatic model yields very good correspondence to the experiment.

Analyzing the excitonic landscape and its full coupling pattern is highly relevant as light-harvesting mechanisms in photosynthetic organisms still have not been fully resolved. Most often, non-adiabatic and non-resonant coupling amplitudes connecting excited molecular states and the ground state are ignored as the exciton lifetime is of the order of nanoseconds (as is recovered in our calculations); however, this may be very significant for understanding photoprotection mechanisms, where exciton lifetime may be tuned to much shorter times in high light conditions. It is also important to point out that the non-adiabaticity is not the only intermolecular vibronic coupling mechanism. Essentially, the environment-related electrostatic interactions induce non-resonant couplings, which are purely electrostatic in origin. This plays a role for pigments in solution, for concentrational quenching, and quantum technologies, where long non-equilibrium state lifetimes are desirable.

While calculations, based on crystallographic protein structure, give satisfactory results for FMO, more accurate calculations would require molecular dynamics simulations, which could yield Hamiltonian fluctuations, corrections of spectral densities, and other factors that are needed to achieve desirable accuracy. Deviation from the experiment is more severe for FCP: the full absorption spectrum shape only roughly matches the experimental absorption spectrum, where a single Chl *a* related Gaussian-shaped peak at 672 nm dominates the experimental absorption, while additional small peaks around 636 nm signify either Chl *c* or molecular vibrations.[67]

FCP structure is highly complex in terms of ligands—in addition to nine Chl molecules, each monomer has seven fucoxanthins, one diadinoxanthin–diatoxanthin, one phosphatidyl-glycerol, and one digalactosyl–diacylglycerol, and chlorophylls are separated by three α-helices. It might be necessary to include additional ligands for more complex LHC cases and/or to model the surrounding environment using QM/MM methodology, as ligand charge distribution might contribute significantly to the excitonic picture, find probable conformations of the protein, and assess environmental contributions as precisely as possible. The excitonic model in Ref. 68 is the first attempt to characterize FCP. In the present study, we find that there are differences in all of the parameters that were modeled: Hamiltonian, relaxation times, and absorption spectra, mostly because of different methodologies: the prior publication used point dipole approximation and planar structures of chlorophylls, while in this paper we used more accurate TrESP methodology and crystallographic structures of chlorophylls; hence, the differences in the excited state interactions of the Hamiltonians appear. Most of the strongest interacting pairs remain the same ($a402$–$a406$, $a401$–$a407$, $a401$–c_1408, and $a406$–c_2403); however, $a406$–c_2403 and $a402$–c_2403 interactions are overestimated by 25 and 36 cm^{-1} compared to our model, respectively. Moreover, the calculations by the Valkunas group were performed *in vacuo*, and the protein environment was not taken into account in any form; therefore, the excitation energies are not comparable: the homogeneous environment of the vacuum allows the Ref. 68 model to form a uniform Gaussian absorption peak in the Chl *a* Q_y region, while environmental factors in the present model induce a shoulder peak near the main Q_y excitation. In both models, the fast transfer between S_1 excited states is obtained, while we get slower transfer between Chl *c* and *a* than in the Ref. 68 model.

Our modeling does not include molecular vibrations, which are quite significant in Chl *a* pigments. While BChl pigments are more weakly coupled to vibrations, they still lead to vibrational sidebands in absorption spectra. Addressing high frequency vibrations in spectra calculations is extremely complicated and requires using more sophisticated theories. A range of exact approaches, e.g., hierarchical equations of motion,[83] time-dependent Dirac–Frenkel variational principle,[89] or stochastic path integrals,[84] can consider such problems; or more targeted approaches like Multi-Configuration Time-Dependent Hartree (MCTDH),[49] n-particle vibronic models[92] can include the high frequency molecular vibrations more efficiently. However, these approaches are computationally very expensive. Overall, high quality vibrations treatment could improve correspondence with the experiment; the main focus of this study is different.

By excluding the high frequency vibrations, we are also unable to address the short lifetimes of S_2 or Q_x states in BChl and Chl pigments. The short lifetimes are inherent in these molecules due to intramolecular non-adiabatic mixing with high frequency vibrations. The correct treatment of this effect requires more detailed quantum analysis of non-adiabaticity in the pigment molecules. They are not included in our model; hence, S_2 state lifetimes are not realistic. However, these contributions should not significantly affect the main features of absorption spectra, especially at the main absorption intensities, which are concentrated at S_1 or Q_y transitions. Hence, our estimation of S_2 or Q_x exciton lifetimes should be considered as the upper limit, while the estimation of S_1 or Q_y lifetimes quite well agrees with the experiment. Demonstration of S_1 and S_2 mixing with vibrations along with environment-induced mixing effects should be significant for excitation dynamics and relaxation pathway analysis, which must be addressed in future studies of pigment–protein complexes.

Vibrational and fluctuation properties of the environment are addressed in the FCP study by Maity *et al.*,[70] which highlights the fact that the combination of QM/MM methodology with the *P. tricornutum* FCP complex leads to similar or even lower excitation energies of Chl *c* than Chl *a*, which highlights that energy transfer in different FCP complexes might be different. In our study, excitation energies were not taken as purely quantities of *ab initio* calculations, but as a shift from a value in solvent absorption resulting from the protein environmental charges. In our model, both Chl *c* experience significant shifts to lower energies; however, they are still ~300 cm^{-1} higher than Chl *a* S_1 absorption energy. The coupling strength between pigments quantitatively agrees, as the strongest couplings are between the same pigment pairs. However, there are significant differences between *c*408–*a*401 and *c*403–*a*406 pairs, as our model tends to find these couplings 2–3 times stronger, even though strong Chl *a* couplings agree quite well numerically between two models. Kleinekathöfer *et al.* included the high-frequency vibrational part of the spectrum and, therefore, obtained good agreement with the experiment; however, non-resonant couplings were ignored.

VI. CONCLUSIONS

Intramolecular mechanisms of non-adiabaticity are related to molecular vibrations.[93] We thus show that intermolecular vibrationless contributions induce additional non-adiabatic-like non-resonant coupling effects, which may be dominating in pigment–protein complexes in determining the excited state lifetime. We have applied our model to two small light-harvesting complexes: FMO, made of BChls, and FCP, made of Chls. The calculated Hamiltonians for these light-harvesting complexes prove that the strongest non-resonant interactions are at least one order of magnitude larger than the interchromophore resonant interactions, going up to 10^3 cm^{-1}; therefore, they cannot be excluded from typical exciton models of light harvesting complexes. The reason for such large values is due to the cumulative effect of all surrounding components: protein, solvent, other pigments, etc. This leads to the estimation of each exciton lifetime, which is of the order of ns—the reasonable value expected from experiments—therefore, demonstrating that the electrostatic non-resonant amplitudes may be the dominant contributions determining excitation lifetime in LHCs. The full S_0, S_1, S_2 model additionally suggests strong cooperation (coherent mixing and incoherent excitation transfer) of S_1 and S_2 excitations, especially in the FCP complex. The non-resonant coupling inclusion also impacts the absorption spectra: it shifts to higher frequencies and changes in band intensity and peak positions. Consequently, the refined exciton models, which exclude non-resonant mixing, may need to be refined. Moreover, the existing relaxation channel between the excited and ground states in this level of theory might lay the foundation to evaluate exciton decay times in more complex LHCs, playing a role in excitation conversion and quenching.

SUPPLEMENTARY MATERIAL

See the supplementary material for FMO (3EOJ PDB structure) Hamiltonian and transfer times, FCP (6A2W PDB structure) and FMO (3EOJ PDB structure) couplings to the ground state, and excitation energy comparison between different models. In addition, more images of the same absorption spectra presented in an article, but block diagonal and full model forms plotted in the same graph for each case of FMO and FCP complexes, are present in the supplementary material.

ACKNOWLEDGMENTS

This research was carried out in the framework of the "Universities' Excellence Initiative" program by the Ministry of Education, Science, and Sports of the Republic of Lithuania under the agreement with the Research Council of Lithuania (Project No. S-A-UEI-23-6) and was funded by the Research Council of Lithuania (Grant No. S-MIP-23-48). Computations were performed on resources at the High Performance Computing Center, HPC Sauletekis, of the Faculty of Physics, Vilnius University.

AUTHOR DECLARATIONS

Conflict of Interest

The authors have no conflicts to disclose.

Author Contributions

Austėja Mikalčiūtė: Data curation (equal); Formal analysis (equal); Investigation (equal); Methodology (equal); Software (equal); Visualization (equal); Writing – original draft (equal); Writing – review & editing (equal). **Darius Abramavičius**: Conceptualization (lead); Formal analysis (equal); Funding acquisition (lead); Investigation (equal); Methodology (equal); Project administration (lead); Software (equal); Supervision (lead); Writing – original draft (equal); Writing – review & editing (equal).

DATA AVAILABILITY

The data that support the findings of this study are available from the corresponding author upon reasonable request.

APPENDIX: GENERIC HAMILTONIAN OF A MOLECULAR COMPLEX

Next, we present expressions for specific coupling elements. First of all, the coupling-induced energy shift is defined by

$$V^{(00)}_{mm'} = \langle g_m g_{m'} | V_{mm'} | g_m g_{m'} \rangle. \tag{A1}$$

In the real space, this is the integral

$$V^{(00)}_{mm'} = \int dr_1^{(m)} dr_1^{(m')} dr_2^{(m)} \dots V_{mm'} \left| \Psi_g^{(m)} \left(\left\{ r_\alpha^{(m)} \right\} \right) \right|^2 \times \left| \Psi_g^{(m')} \left(\left\{ r_\alpha^{(m')} \right\} \right) \right|^2, \tag{A2}$$

where $V_{mm'}$ is defined in Eq. (4). It is a sum over Coulomb interaction kernels where each term depends on a single electron coordinates in one molecule. Keeping in mind that electron re-labeling does not change the wavefunction, the relevant quantity that enters the coupling integral is the total charge density of the mth molecule in its ground state

$$\sigma_m^{(00)}(\boldsymbol{r}) = -eK \int dr_2^{(m)} dr_3^{(m)} \dots \left| \Psi_g^{(m)}(\boldsymbol{r}, \boldsymbol{r}_2 \boldsymbol{r}_3 \dots \boldsymbol{r}_K) \right|^2 + \sum_n^N e q_n \delta\left(\boldsymbol{r} - \boldsymbol{R}_n^{(m)}\right), \tag{A3}$$

and excited state

$$\sigma_m^{(11)}(\boldsymbol{r}) = -eK \int dr_2^{(m)} dr_3^{(m)} \dots \left| \Psi_e^{(m)}(\boldsymbol{r}, \boldsymbol{r}_2 \boldsymbol{r}_3 \dots \boldsymbol{r}_K) \right|^2 + \sum_n^N e q_n \delta\left(\boldsymbol{r} - \boldsymbol{R}_n^{(m)}\right), \tag{A4}$$

with e being the electron elementary charge, leading to the coupling-induced energy shift,

$$V^{(00)}_{mm'} = \iint_V dr dr' \frac{\sigma_m^{(00)}(\boldsymbol{r}) \sigma_{m'}^{(00)}(\boldsymbol{r}')}{|\boldsymbol{r} - \boldsymbol{r}'|}. \tag{A5}$$

Similarly, we can write all other matrix elements, such as

$$V^{(10)}_{mm'} = \iint_V dr dr' \frac{\sigma_m^{(11)}(\boldsymbol{r}) \sigma_{m'}^{(00)}(\boldsymbol{r}')}{|\boldsymbol{r} - \boldsymbol{r}'|}, \tag{A6}$$

and the resonant coupling

$$J_{mm'} = \iint_V dr dr' \frac{\sigma_m^{(10)}(\boldsymbol{r}) \sigma_{m'}^{(01)}(\boldsymbol{r}')}{|\boldsymbol{r} - \boldsymbol{r}'|}, \tag{A7}$$

where we use the transition charge density, which is the electronic-only property,

$$\sigma_m^{(10)}(\boldsymbol{r}) = -eK \int dr_2^{(m)} dr_3^{(m)} \dots \Psi_e^{(m)}(\boldsymbol{r}, \boldsymbol{r}_2 \boldsymbol{r}_3 \dots \boldsymbol{r}_K) \times \Psi_g^{(m)}(\boldsymbol{r}, \boldsymbol{r}_2 \boldsymbol{r}_3 \dots \boldsymbol{r}_K). \tag{A8}$$

The difference of these couplings is important for the exciton Hamiltonian, as it can be written via the difference in charge density,

$$V^{(10)}_{mm'} - V^{(00)}_{mm'} = \iint_V dr dr' \frac{\left(\sigma_m^{(11)}(\boldsymbol{r}) - \sigma_m^{(00)}(\boldsymbol{r})\right) \sigma_{m'}^{(00)}(\boldsymbol{r}')}{|\boldsymbol{r} - \boldsymbol{r}'|}. \tag{A9}$$

Notice that due to the orthogonality of different wave functions, we have

$$\int d r \sigma_m^{(10)}(\boldsymbol{r}) = 0. \tag{A10}$$

Finally, the non-resonant coupling connecting the ground state and the excited state of molecule k is due to

$$L_k = \sum_m \iint d\mathbf{r} d\mathbf{r}' \frac{\sigma_k^{(10)}(\mathbf{r}) \sigma_m^{(00)}(\mathbf{r}')}{|\mathbf{r} - \mathbf{r}'|}. \tag{A11}$$

If the molecules have several excited states (1 and 2), the environment induces electrostatic coupling between these excited states (which are uncoupled in a vacuum). One has a similar expression involving the transition charge density between these excited states

$$L_k^{(21)} = \sum_m \iint d\mathbf{r} d\mathbf{r}' \frac{\sigma_k^{(21)}(\mathbf{r}) \sigma_m^{(00)}(\mathbf{r}')}{|\mathbf{r} - \mathbf{r}'|}, \tag{A12}$$

with

$$\sigma_m^{(21)}(\boldsymbol{r}) = -eK \int dr_2^{(m)} dr_3^{(m)} \dots \Psi_{e_2}^{(m)}(\boldsymbol{r}, \boldsymbol{r}_2 \boldsymbol{r}_3 \dots \boldsymbol{r}_K) \times \Psi_{e_1}^{(m)}(\boldsymbol{r}, \boldsymbol{r}_2 \boldsymbol{r}_3 \dots \boldsymbol{r}_K). \tag{A13}$$

REFERENCES

[1] R. Blankenship, *Molecular Mechanism of Photosynthesis* (Blackwell Science, Oxford, UK, 2001), Vol. 11, ISBN: 978-0632043217.

[2] A. Ruban, *The Photosynthetic Membrane* (John Wiley and Sons, Ltd., 2012), ISBN: 9781118447628.

[3] H. Zhou, T. Fan, and D. Zhang, "An insight into artificial leaves for sustainable energy inspired by natural photosynthesis," ChemCatChem **3**(3), 513–528 (2011).

[4] P. J. D. Janssen, M. D. Lambreva, N. Plumeré *et al.*, "Photosynthesis at the forefront of a sustainable life," Front. Chem. **2**, 36 (2014).

[5] S. I. Allakhverdiev, "Artificial photosynthesis: Powering a green new deal for sustainable energy," Int. J. Hydrogen Energy **90**, 199–209 (2024).

[6] G. S. Schlau-Cohen, "Principles of light harvesting from single photosynthetic complexes," Interface Focus **5**, 20140088 (2015).

[7] M. L. Groot, N. P. Pawlowicz, L. J. G. W. van Wilderen *et al.*, "Initial electron donor and acceptor in isolated Photosystem II reaction centers identified with femtosecond mid-IR spectroscopy," Proc. Natl. Acad. Sci. U. S. A. **102**(37), 13087–13092 (2005).

[8] J. A. Myers, K. L. M. Lewis, F. D. Fuller *et al.*, "Two-dimensional electronic spectroscopy of the D1-D2-cyt b559 photosystem II reaction center complex," J. Phys. Chem. Lett. **1**(19), 2774–2780 (2010).

[9] X. J. Jordanides, G. D. Scholes, and G. R. Fleming, "The mechanism of energy transfer in the bacterial photosynthetic reaction center," J. Phys. Chem. B **105**(8), 1652–1669 (2001).

[10] S. Dracheva, J. C. Williams, and R. e. Blankenship, *Research in Photosynthesis* (Kluwer Academic Publishers, Dordrecht, The Netherlands, 1992).

[11] X. Pan, P. Cao, X. Su *et al.*, "Structural analysis and comparison of light-harvesting complexes I and II," Biochim. Biophys. Acta, Bioenerg. **1861**(4), 148038 (2020).

[12] S. Jansson, "The light-harvesting chlorophyll ab-binding proteins," Biochim. Biophys. Acta, Bioenerg. **1184**(1), 1–19 (1994).

[13] T. Polívka and H. A. Frank, "Molecular factors controlling photosynthetic light harvesting by carotenoids," Acc. Chem. Res. **43**(8), 1125–1134 (2010).

[14] A. J. Simkin, L. Kapoor, C. G. P. Doss *et al.*, "The role of photosynthesis related pigments in light harvesting, photoprotection and enhancement of photosynthetic yield in planta," Photosynth. Res. **152**(1), 23–42 (2022).

[15] A. Sharma, P. Singh, and P. Srivastava, "Insights into the world of diatoms: From essentials to applications, chapter photosynthetic pigments," in *Diatoms* (Springer Nature, Singapore, 2023), pp. 1–20, ISBN: 978-981-19-5920-2.

[16] B. W. Matthews, R. E. Fenna, M. C. Bolognesi *et al.*, "Structure of a bacteriochlorophyll *a*-protein from the green photosynthetic bacterium *Prosthecochloris aestuarii*," J. Mol. Biol. **131**(2), 259–285 (1979).

[17] X. Lu, B. Selvaraj, S. Ghimire-Rijal *et al.*, "Neutron and X-ray analysis of the Fenna–Matthews–Olson photosynthetic antenna complex from *Prosthecochloris aestuarii*," Acta Crystallogr., Sect. F: Struct. Biol. Commun. **75**, 171–175 (2019).

[18] P. Qian, D. J. K. Swainsbury, T. I. Croll *et al.*, "Cryo-EM structure of the *Rhodobacter sphaeroides* light-harvesting 2 complex at 2.1 Å," Biochemistry **60**(44), 3302–3314 (2021).

[19] W. Wang, L.-J. Yu, C. Xu *et al.*, "Structural basis for blue-green light harvesting and energy dissipation in diatoms," Science **363**, eaav0365 (2019).

[20] J. Adolphs, F. Müh, M. E. A. Madjet *et al.*, "Structure-based calculations of optical spectra of photosystem I suggest an asymmetric light-harvesting process," J. Am. Chem. Soc. **132**(10), 3331–3343 (2010).

[21] T. Renger, I. Trostmann, C. Theiss *et al.*, "Refinement of a structural model of a pigment–protein complex by accurate optical line shape theory and experiments," J. Phys. Chem. B **111**(35), 10487–10501 (2007).

[22] F. Müh, M. E.-A. Madjet, and T. Renger, "Structure-based simulation of linear optical spectra of the CP43 core antenna of photosystem II," Photosynth. Res. **111**(1–2), 87–101 (2012).

[23] O. Rancova, J. Sulskus, and D. Abramavicius, "Insight into the structure of photosynthetic LH2 aggregate from spectroscopy simulations," J. Phys. Chem. B **116**(27), 7803–7814 (2012).

[24] Y. Song, R. Sechrist, H. H. Nguyen *et al.*, "Excitonic structure and charge separation in the heliobacterial reaction center probed by multispectral multidimensional spectroscopy," Nat. Commun. **12**(1), 2801 (2021).

[25] K. L. M. Lewis, F. D. Fuller, J. A. Myers *et al.*, "Simulations of the two-dimensional electronic spectroscopy of the photosystem II reaction center," J. Phys. Chem. A **117**(1), 34–41 (2013).

[26] R. E. Fenna and B. W. Matthews, "Chlorophyll arrangement in a bacteriochlorophyll protein from *Chlorobium limicola*," Nature **258**, 573–577 (1975).

[27] J. M. Olson, "The FMO protein," Photosynth. Res. **80**, 181–187 (2004).

[28] V. Gulbinas, L. Valkunas, D. Kuciauskas *et al.*, "Singlet–singlet annihilation and local heating in FMO complexes," J. Phys. Chem. **100**(45), 17950–17956 (1996).

[29] S. G. Johnson and G. J. Small, "Excited-state structure and energy-transfer dynamics of the bacteriochlorophyll *a* antenna complex from *Prosthecochloris aestuarii*," J. Phys. Chem. **95**(1), 471–479 (1991).

[30] R. J. W. Louwe and T. J. Aartsma, "On the nature of energy transfer at low temperatures in the BChl *a* pigment-protein complex of green sulfur bacteria," J. Phys. Chem. B **101**(37), 7221–7226 (1997).

[31] V. I. Prokhorenko, A. R. Holzwarth, F. R. Nowak, and T. J. Aartsma, "Growing-in of optical coherence in the FMO antenna complexes," J. Phys. Chem. B **106**(38), 9923–9933 (2002).

[32] A. Khmelnitskiy, R. G. Saer, R. E. Blankenship, and R. Jankowiak, "Excitonic energy landscape of the Y16F mutant of the *Chlorobium tepidum* Fenna–Matthews–Olson (FMO) complex: High resolution spectroscopic and modeling studies," J. Phys. Chem. B **122**(14), 3734–3743 (2018).

[33] A. Kell, K. Acharya, V. Zazubovich, and R. Jankowiak, "On the controversial nature of the 825 nm exciton band in the FMO protein complex," J. Phys. Chem. Lett. **5**(8), 1450–1456 (2014).

[34] S. I. E. Vulto, M. A. De Baat, R. J. W. Louwe *et al.*, "Exciton simulations of optical spectra of the FMO complex from the green sulfur bacterium *Chlorobium tepidum* at 6 K," J. Phys. Chem. B **102**(47), 9577–9582 (1998).

[35] S. Georgakopoulou, R. J. Cogdell, R. Van Grondelle, and H. van Amerongen, "Linear-dichroism measurements on the LH2 antenna complex of *Rhodopseudomonas acidophila* strain 10050 show that the transition dipole moment of the carotenoid rhodopin glucoside is not collinear with the long molecular axis," J. Phys. Chem. B **107**(3), 655–658 (2003).

[36] M. Wendling, M. Przyjalgowski, D. Gülen *et al.*, "The quantitative relationship between structure and polarized spectroscopy in the FMO complex of *Prosthecochloris aestuarii*: Refining experiments and simulations," Photosynth. Res. **71**, 99–123 (2002).

[37] J. Adolphs and T. Renger, "How proteins trigger excitation energy transfer in the FMO complex of green sulfur bacteria," Biophys. J. **91**(8), 2778–2797 (2006).

[38] Y. Kim, D. Morozov, V. Stadnytskyi *et al.*, "Predictive first-principles modeling of a photosynthetic antenna protein: The Fenna–Matthews–Olson complex," J. Phys. Chem. Lett. **11**(5), 1636–1643 (2020).

[39] Z. Huai, Z. Tong, Y. Mei, and Y. Mo, "Theoretical study of the spectral differences of the Fenna–Matthews–Olson protein from different species and their mutants," J. Phys. Chem. B **125**(30), 8313–8324 (2021).

[40] T. Reinot, A. Khmelnitskiy, A. Kell *et al.*, "Exciton lifetime distributions and population dynamics in the FMO protein complex from *Prosthecochloris aestuarii*," ACS Omega **6**(8), 5990–6008 (2021).

[41] E. Thyrhaug, R. Tempelaar, M. J. P. Alcocer *et al.*, "Identification and characterization of diverse coherences in the Fenna–Matthews–Olson complex," Nat. Chem. **10**(7), 780–786 (2018).

[42] E. Thyrhaug, K. Žídek, J. Dostál *et al.*, "Exciton structure and energy transfer in the Fenna–Matthews–Olson complex," J. Phys. Chem. Lett. **7**(9), 1653–1660 (2016).

[43] J. A. Myers, K. L. M. Lewis, P. F. Tekavec, and J. P. Ogilvie, "Two-color two-dimensional Fourier transform electronic spectroscopy with a pulse-shaper," Opt. Express **16**(22), 17420–17428 (2008).

[44] G. S. Engel, T. R. Calhoun, E. L. Read *et al.*, "Evidence for wavelike energy transfer through quantum coherence in photosynthetic systems," Nature **446**(7137), 782–786 (2007).

[45] D. Zigmantas and T. Mancal, "Ultrafast two-dimensional spectroscopy of photosynthetic systems," in *Ultrafast Electronic and Structural Dynamics* (Springer, 2024), pp. 355–396, ISBN: 978-981-97-2913-5.

[46] L. Wang, M. A. Allodi, and G. S. Engel, "Quantum coherences reveal excited-state dynamics in biophysical systems," Nat. Rev. Chem. **3**, 477–490 (2019).

[47] V. Butkus, D. Zigmantas, L. Valkunas, and D. Abramavicius, "Vibrational vs. electronic coherences in 2D spectrum of molecular systems," Chem. Phys. Lett. **545**, 40–43 (2012).

[48] V. Butkus, J. Alster, E. Bašinskaitė *et al.*, "Discrimination of diverse coherences allows identification of electronic transitions of a molecular nanoring," J. Phys. Chem. Lett. **8**(10), 2344–2349 (2017).

[49] M. Schröter, S. Ivanov, J. Schulze *et al.*, "Exciton–vibrational coupling in the dynamics and spectroscopy of Frenkel excitons in molecular aggregates," Phys. Rep. **567**, 1–78 (2015), part of the Special Issue: Exciton–vibrational coupling in the dynamics and spectroscopy of Frenkel excitons in molecular aggregates.

[50] Schrödinger, LLC, The PyMOL Molecular Graphics System, version 1.8, 2015.

[51] R. Dennington, T. A. Keith, and J. M. Millam, GaussView Version 6, Semichem, Inc., Shawnee Mission KS, 2019.

[52] M. J. Frisch, G. W. Trucks, H. B. Schlegel *et al.*, *Gaussian 16, Revision C.01*, Gaussian, Inc., Wallingford, CT, 2016.

[53] T. Lu and F. Chen, "Multiwfn: A multifunctional wavefunction analyzer," J. Comput. Chem. **33**(5), 580–592 (2012).

[54] E. F. Pettersen, T. D. Goddard, C. C. Huang *et al.*, "UCSF Chimera—A visualization system for exploratory research and analysis," J. Comput. Chem. **25**(13), 1605–1612 (2004).

[55] R. S. Knox and B. Q. Spring, "Dipole strengths in the chlorophylls," Photochem. Photobiol. **77**, 497–501 (2003).

[56] D. E. Tronrud, J. Wen, L. Gay, and R. E. Blankenship, "The structural basis for the difference in absorbance spectra for the FMO antenna protein from various green sulfur bacteria," Photosynth. Res. **100**(2), 79–87 (2009).

[57] E. Jurrus, D. Engel, K. Star *et al.*, "Improvements to the APBS biomolecular solvation software suite," Protein Sci. **27**(1), 112–128 (2018).

[58] D. Sitkoff, K. A. Sharp, and B. Honig, "Accurate calculation of hydration free energies using macroscopic solvent models," J. Phys. Chem. **98**(7), 1978–1988 (1994).

[59] D. A. Case *et al.*, "AmberTools," J. Chem. Inf. Model. **63**(20), 6183–6191 (2023).

[60] X. Pi, S. Zhao, W. Wang *et al.*, "The pigment-protein network of a diatom photosystem II–light-harvesting antenna supercomplex," Science **365**(6452), eaax4406 (2019).

[61] C. Büchel, "Fucoxanthin-chlorophyll-proteins and non-photochemical fluorescence quenching of diatoms," in *Non-Photochemical Quenching and Energy Dissipation in Plants, Algae and Cyanobacteria* (Springer, The Netherlands, 2014), pp. 259–275, ISBN: 978-94-017-9031-4.

[62] P. Kuczyńska, M. Jemiola-Rzeminska, and K. Strzalka, "Photosynthetic pigments in diatoms," Mar. Drugs **13**, 5847–5881 (2015).

[63] R. G. West, D. Bína, M. Fuciman *et al.*, "Ultrafast multi-pulse transient absorption spectroscopy of fucoxanthin chlorophyll *a* protein from *Phaeodactylum tricornutum*," Biochim. Biophys. Acta, Bioenerg. **1859**, 357–365 (2018).

[64] V. Butkus, A. Gelzinis, R. Augulis *et al.*, "Coherence and population dynamics of chlorophyll excitations in FCP complex: Two-dimensional spectroscopy study," J. Chem. Phys. **142**, 212414 (2015).

[65] E. Songaila, R. Augulis, A. Gelzinis *et al.*, "Ultrafast energy transfer from chlorophyll c_2 to chlorophyll *a* in fucoxanthin–chlorophyll protein complex," J. Phys. Chem. Lett. **4**(21), 3590–3595 (2013).

[66] C. B. Field, M. J. Behrenfeld, J. T. Randerson, and P. Falkowski, "Primary production of the biosphere: Integrating terrestrial and oceanic components," Science **281**(5374), 237–240 (1998).

[67] C. Büchel, "Fucoxanthin-chlorophyll proteins in diatoms: 18 and 19 kDa subunits assemble into different oligomeric states," Biochemistry **42**(44), 13027–13034 (2003).

[68] A. Mikalčiūtė *et al.*, "Structure-based model of fucoxanthin–chlorophyll protein complex: Calculations of chlorophyll electronic couplings," J. Chem. Phys. **156**, 234101 (2022).

[69] M. Tsujimura, M. Sugano, H. Ishikita, and K. Saito, "Mechanism of absorption wavelength shift depending on the protonation state of the acrylate group in chlorophyll *c*," J. Phys. Chem. B **127**(2), 505–513 (2023).

[70] S. Maity, V. Daskalakis, T. L. C. Jansen, and U. Kleinekathöfer, "Electric field susceptibility of chlorophyll c leads to unexpected excitation dynamics in the major light-harvesting complex of diatoms," J. Phys. Chem. Lett. **15**(9), 2499–2510 (2024).

[71] C. Büchel, "Light harvesting complexes in chlorophyll *c*-containing algae," Biochim. Biophys. Acta, Bioenerg. **1861**(4), 148027 (2020).

[72] C. Weiss, "The Pi electron structure and absorption spectra of chlorophylls in solution," J. Mol. Spectrosc. **44**, 37–80 (1972).

[73] M. Taniguchi and J. S. Lindsey, "Absorption and fluorescence spectral database of chlorophylls and analogues," Photochem. Photobiol. **97**(1), 136–165 (2021).

[74] H. Du, R.-C. A. Fuh, J. Li *et al.*, "PhotochemCAD: A computer-aided design and research tool in photochemistry," Photochem. Photobiol. **68**(2), 141–142 (1998).

[75] M. W. Fawley, "A new form of chlorophyll *c* involved in light-harvesting," Plant Physiol. **91**(2), 727–732 (1989).

[76] L. Valkunas, D. Abramavicius, and T. Mančal, *Molecular Excitation Dynamics and Relaxation* (John Wiley and Sons, Ltd., 2013), ISBN: 9783527653652.

[77] V. May and O. Kühn, *Charge and Energy Transfer Dynamics in Molecular Systems* (John Wiley and Sons, Ltd., 2011), ISBN: 9783527633791.

[78] D. Abramavicius, B. Palmieri, D. V. Voronine *et al.*, "Coherent multidimensional optical spectroscopy of excitons in molecular aggregates; quasiparticle versus supermolecule perspectives," Chem. Rev. **109**(6), 2350–2408 (2009).

[79] L. Cupellini, F. Lipparini, and J. Cao, "Absorption and circular dichroism spectra of molecular aggregates with the full cumulant expansion," J. Phys. Chem. B **124**(39), 8610–8617 (2020).

[80] S. Nakajima, "On quantum theory of transport phenomena: Steady diffusion," Prog. Theor. Phys. **20**(6), 948–959 (1958).

[81] R. Zwanzig, "Ensemble method in the theory of irreversibility," J. Chem. Phys. **33**(5), 1338–1341 (1960).

[82] F. Shibata, Y. Takahashi, and N. Hashitsume, "A generalized stochastic Liouville equation. Non-Markovian versus memoryless master equations," J. Stat. Phys. **17**(4), 171–187 (1977).

[83] A. Ishizaki and G. R. Fleming, "Unified treatment of quantum coherent and incoherent hopping dynamics in electronic energy transfer: Reduced hierarchy equation approach," J. Chem. Phys. **130**(23), 234111 (2009).

[84] J. M. Moix, J. Ma, and J. Cao, "Förster resonance energy transfer, absorption and emission spectra in multichromophoric systems. III. Exact stochastic path integral evaluation," J. Chem. Phys. **142**(9), 094108 (2015).

[85] A. Gelzinis, D. Abramavicius, and L. Valkunas, "Absorption lineshapes of molecular aggregates revisited," J. Chem. Phys. **142**(15), 154107 (2015).

[86] M. Cho, H. M. Vaswani, T. Brixner *et al.*, "Exciton analysis in 2D electronic spectroscopy," J. Phys. Chem. B **109**(21), 10542–10556 (2005).

[87] J. Ma and J. Cao, "Förster resonance energy transfer, absorption and emission spectra in multichromophoric systems. I. Full cumulant expansions and system-bath entanglement," J. Chem. Phys. **142**(9), 094106 (2015).

[88] D. Abramavicius, V. Chorošajev, and L. Valkunas, "Tracing feed-back driven exciton dynamics in molecular aggregates," Phys. Chem. Chem. Phys. **20**, 21225–21240 (2018).

[89] M. Jakučionis, A. Žukas, and D. Abramavičius, "Modeling molecular J and H aggregates using multiple-Davydov D2 ansatz," Phys. Chem. Chem. Phys. **24**, 17665–17672 (2022).

[90] S. Mukamel, *Principles of Nonlinear Optical Spectroscopy* (Oxford University Press, New York, 1995).

[91] B. González-Soria, F. Delgado, and A. Anaya-Morales, "Parametric mapping of quantum regime in Fenna–Matthews–Olson light-harvesting complexes: A synthetic review of models, methods and approaches," Appl. Sci. **10**, 6474 (2020).

[92] V. Bubilaitis, O. Rancova, and D. Abramavicius, "Vibration-mediated energy transport in bacterial reaction center: Simulation study," J. Chem. Phys. **154**(21), 214115 (2021).

[93] F. Caycedo-Soler, A. Mattioni, J. Lim *et al.*, "Exact simulation of pigment-protein complexes unveils vibronic renormalization of electronic parameters in ultrafast spectroscopy," Nat. Commun. **13**(1), 2912 (2022).